



Malate-based polyester chemically shielded metal-phenolic networks coated artificial hair fibers with long-lasting antimicrobial and anti-inflammatory performance

Yue Li^{a,b,1}, Yong Miao^{a,1}, Lunan Yang^{a,1}, Gaofeng Wang^a, Meimei Fu^{a,b}, Yue Wang^{a,b}, Danlan Fu^a, Junfei Huang^a, Jin Wang^a, Zhexiang Fan^a, Zhihui Lu^{a,c,*}, Jinshan Guo^{a,b,*}, Zhiqi Hu^{a,*}

^a Department of Plastic and Aesthetic Surgery, Nanfang Hospital of Southern Medical University, Department of Histology and Embryology, NMPA Key Laboratory for Safety Evaluation of Cosmetics, School of Basic Medical Sciences, Southern Medical University, Guangzhou 510515, PR China

^b Guangdong Provincial Key Laboratory of Bone and Joint Degeneration Diseases, The Third Affiliated Hospital of Southern Medical University, Guangzhou 510630, PR China

^c Regenerative Medicine and Tissue Repair Research Center, Huangpu Institute of Materials, Guangzhou 510530, PR China

ARTICLE INFO

Keywords:

Metal-phenolic networks
Antibacterial coating
Silver
Anti-inflammatory
Malate-based polymer

ABSTRACT

Microbially induced peri-implant infection and dislodgement are among the most common complications of implant surgery. Most existing medical implant surfaces lack long-lasting antimicrobial capacity and are adversely affected by excessive reactive oxygen species production or burst release of antimicrobial agents within short periods. This study aimed to perform in situ reduction and anchoring of silver nanoparticles (AgNPs) on polyamide (PA) surfaces pre-deposited with tannic acid (TA) coating and the multicycle deposition of tannin-silver (TA-Ag) metal-phenolic networks (MPNs). Through in situ reduction of silver ions (Ag^+) by plant-derived tannic acid, TA-Ag MPNs were deposited on polyamide in a multicycle manner, and the remaining functionalities on the immobilized TA moieties were subsequently covalently linked to poly(1,8-octanediol L-malate) (POM), a malate-based biodegradable polymer. The AgNPs were effectively locked in the coating matrix comprising MPNs and POM via coordination bonds between AgNPs and tannin and covalent crosslinks between tannin and POM, which slowed down the “burst release” of AgNPs and extended the release time of Ag^+ (up to 56 days). The remarkable long-term antibacterial (>97 %) and anti-inflammatory coating have promising widespread applications not only in artificial hair fibers but also in other medical implant applications.

1. Introduction

Infections associated with bacteria and biofilms are a problematic issue, especially in the field of medical implants [1]. Implant-associated infections (IAIs) often lead to medical implant failure and eventually require implant removal, causing secondary injuries and psychophysical burdens to patients. To address the clinical issues caused by bacterial infections on medically implanted devices, antibacterial coatings are drawing increasing attention due to their promising capacity to prevent bacterial growth and subsequent biofilm adhesion on the

surface of implanted devices [2,3]. Several types of coating materials (antibiotics-based, PDA-based, plasma polymer-based, graphene-based, metal-based, etc.) have been explored and applied in functional antibacterial coating design, and the facile synthesis of antibacterial coating materials that attach to substrate surfaces varies from inorganic to organic, and substrates coatings with high antibiotics or drug loads. However, the antimicrobial properties can be severely hindered by several challenges including a short antibacterial duration and substrate-dependent and redundant synthesis processes [4–12]. Silver has held an important position in the history of antibacterial compound

Abbreviations: AFM, Atomic force microscopy; FBR, Foreign body response; HUVEC, Human Umbilical Vein Endothelial Cells; MA, Malic acid; PBS, Phosphate buffer saline; PE, Plasma-optical emission; ROS, Reactive oxygen species; TCA, Tricarboxylic acid; TSB, Tryptic soy broth; XPS, X-ray Photoelectron Spectroscopy.

* Corresponding authors.

E-mail addresses: sanlumo12@smu.edu.cn (Z. Lu), jsguo4127@smu.edu.cn (J. Guo), huzhiqidr163@i.smu.edu.cn (Z. Hu).

¹ Y. Li, Y. Miao and L. Yang contributed equally to this work.

<https://doi.org/10.1016/j.cej.2022.140572>

Received 12 September 2022; Received in revised form 17 November 2022; Accepted 21 November 2022

Available online 23 November 2022

1385-8947/© 2022 The Author(s). Published by Elsevier B.V. This is an open access article under the CC BY-NC-ND license (<http://creativecommons.org/licenses/by-nc-nd/4.0/>).

development [13]. It has a broad-spectrum antibacterial effect and is widely used in various areas such as skin repair, bone regeneration, medical devices, and other fields. It is applied as a component to modify implant surfaces in various antibacterial coating materials [14–17]. However, the main limitations of the use of silver-containing coatings include an unpredictable silver ion release kinetic curve, single antibacterial function, substrate-dependency, use of environmentally unfriendly organic solvents, short duration, and unstable antibacterial activity [18–21]. In addition, although the mechanism underlying the biological activity of silver has not been fully explored, silver nanoparticles have been shown to induce nanotoxicity [22–24]. Further, silver ions (Ag^+) may also induce the expression of a downstream cascade biological actions of chemokines and inflammatory factors (IL-1, IL-8, IL-12, IL-1 β , and TNF- α , among others) by stimulating the production of reactive oxygen species (ROS), resulting in immoderate inflammation in cells and tissues [25–28]. Therefore, it is necessary to rationally functionalize silver according to its application scenarios to reduce its side effects while retaining its antibacterial efficacy [29].

Nature is a source and inspiration for the design and development of multifunctional materials with unique properties and structures [30,31]. Polyphenols derived from natural plants and fruits are known for their good biocompatibility, antibacterial properties, and antioxidant capacity [32]. In recent years, polyphenols have become increasingly popular among researchers and are used in the preparation of coating materials for surface engineering [33,34]. Similar to the mussel-inspired adhesion strategy, plant-derived tannins possess a strong non-specific binding and adhesion ability to various substrates because of their polyphenolic hydroxyl structure [35,36]. In addition, the abundant electron pairs prevalent in the phenolic hydroxyl groups endow TA with a strong ability to scavenge free radicals, enabling it to reduce Ag^+ in situ to form AgNPs [37,38]. The TA-AgNPs-based metal-phenolic networks (MPNs) can effectively moderate the potential toxicity of silver and slow down the release velocity of Ag^+ . Further, during the use of medical implants, coatings composed of inorganic substances may have some defects (such as burst ion release profiles and poor durability), which can hamper their use. In contrast, polymeric organic coatings have attributes such as degradability, biocompatibility, durability, self-healability, and the ability to mediate cellular responses, such as adhesion, proliferation, and differentiation [20,39–42]. Therefore, organic polymer coatings may alleviate the disadvantages of inorganic coatings in implant surface modifications.

Therefore, ideal composite coatings for implant surface modification should have properties including antibacterial activity, controllability, durability, stability, and versatility [2]. This study aimed to in situ reduction and anchoring of AgNPs on polyamide surfaces pre-deposited with a TA coating and deposited TA-AgNPs-based MPNs in multiple cycles. The immobilized TA molecules on TA-AgNPs coating retained multiple unreacted hydroxyl groups, which enables further covalent bonding with the carboxylic acid groups in the POM prepolymer to form a tannin-bridged inorganic–organic composite TA-AgNPs-POM (TAP) coating. The AgNPs were stably anchored in the TAP coating under the dual action of the MPNs and the cross-linking system of tannins and POM [17,43]. Through the dual functional modification of AgNPs, this modification strategy well improves the biocompatibility of the coating without significantly affecting the antibacterial properties. As a result, the antibacterial duration of the coating was greatly increased while the toxicity of the AgNPs was reduced. Further, the antioxidant tannins in the TAP coating can effectively moderate the excess ROS generated by AgNPs and play an anti-inflammatory role. Based on the composite coating formed by the inorganic and organic phases of the MPNs and POM polymer, respectively, a comprehensive in vitro characterization (for composition, micromorphology, hydrophilicity, and roughness, among other properties) of the obtained TAP composite coating was performed. Further, the biocompatibility, antioxidant ability, and antimicrobial performance of the coating were investigated in vitro. In addition, the anti-inflammatory properties were evaluated and a

subcutaneous infection model was constructed to test the antimicrobial efficacy of the coatings in vivo. The fibers were implanted on the scalp of rats to establish an artificial hair implant model. The results indicate that the organic–inorganic bidirectional cooperative TAP composite coating may have broad application prospects in the field of medical implants.

2. Material and methods

2.1. Materials

Tannic acid (TA), L-malic acid (L-MA), 1,8-octanediol, 1,4-dioxane, and Tris-base were obtained from Sigma-Aldrich Co., Ltd. Silver nitrate (AgNO_3) was provided by the Southern Medical University Hazardous Materials Repository Center. Polyamide (PA) membranes (4×4 cm size, 1.5 μm thick) were acquired from the Zhejiang Taizhou Luqiao Sijia Biochemical Plastic Factory. Artificial hair fiber was purchased from Shenzhen Tianlin Industrial Co.

2.2. Preparation

The PA films were 5×5 cm in size and 1.5 mm thick and were cut into multiple disks with a diameter of 1.5 cm for preparation for the following experiment. First, the PA films were ultrasonically cleaned three times with ethanol solution (75 %), followed by a final round of ultrasonic cleaning with deionized water, and the PA films were subsequently left to dry naturally in the air before preparing the composite coatings. The Tris- HNO_3 buffer solution was prepared by mixing Tris-base and HNO_3 solutions, and the pH was adjusted to 8.5 using 0.1 mol/L HNO_3 solutions.

2.3. Synthesis of TA-AgNPs nanocoatings

TA (3.75 g) and AgNO_3 (0.03 g) were weighed and dissolved in 250 mL and 200 mL of Tris- HNO_3 buffer (pH 8.5), respectively. Next, the PA disks were immersed in TA solution and stirred for 12 h. After the deposition of TA, the disks were removed using forceps and rinsed with Tris- NO_3 buffer, followed by stirring in AgNO_3 solution for 10 min. Subsequently, the disks were deposited sequentially using a cycle of TA solution and AgNO_3 solution, with soaking in each solution for 10 min. Each cycle was considered a round and TA-Ag(n) coatings were prepared for the different number of cycles ($n = 1, 3, 5$).

2.4. Synthesis of poly(1,8-octanediol malate) prepolymer

L-malic acid (20.11 g, 0.15 mol) and 1,8-octanediol (14.62 g, 0.10 mol) were weighed in a round bottom flask, and the L-malic acid and 1,8-octanediol were heated and stirred in an oil bath at 140 °C. After both reagents were melted completely, the temperature was moderately adjusted to 120 °C to enable the full esterification of L-malic acid and 1,8-octanediol. After ~ 22 –24 h of continuous reaction, the organic solvent dioxane was added to dissolve the fully reacted POM prepolymer. After another 2–3 h of heating, the mixture was poured into deionized water twice to enable water sedimentation to remove the incompletely reacted compounds and the remnant short-chain prepolymer. The POM prepolymer obtained after the preparation was placed in a refrigerator at -20 °C for subsequent preparation.

2.5. Synthesis of TA-AgNP-POM coatings

The POM prepolymer was dissolved into 1,4-dioxane into a concentration of 10 %, and the prepared TA-Ag5 disks were dipped in the POM prepolymer solution with fine tweezers, and subsequently placed vertically in a 24-well plate to dry naturally. After the surface was air-dried, the disk was placed in a Teflon dish and placed in an oven for 3 days under vacuum heating at 120 °C. Uniformly deposited TA-Ag-POM (TAP) composite coatings were obtained on the surface of the PA

disks. The same method was used to synthesize the coating on artificial hair fibers made of medical PA.

2.6. Characterization of coatings

Several analytical methods were used to characterize the morphology and properties of the composite coatings. Scanning electron microscopy (SEM; ZEISS Gemini 300, Germany) was used to observe the morphology of the coatings, and an energy spectrometer (EDS) attached to the electron microscope was used to analyze the elemental species and percentages of the coating surfaces. Atomic force microscopy (AFM; Oxford Cypher ES, USA) was used to observe the surface morphology of the coatings and their roughness. The chemical structures of coatings were characterized using a Fourier transform attenuated total reflectance infrared spectrometer (ATR-FTIR; Nicolet iS 10, USA) and an ultraviolet–visible spectrophotometer (UV-1800, Mapara, China). The elemental composition and occupancy of the coatings were analyzed and determined using X-ray photoelectron spectroscopy (XPS, Thermo Kalpha, USA). Inductively coupled plasma–optical emission spectrometry (ICP-OES; PerkinElmer 8300, USA) was used to evaluate the release profile of Ag^+ . A contact angle meter (JY-82B Kruss DSA, China) was used to characterize the degree of hydrophobicity of the coating.

2.7. Analysis of Ag^+ release

To investigate the release of Ag^+ from the composite coatings under different time points, the samples (0.05 g) were immersed in phosphate buffer saline (PBS; pH 7.4). At different time intervals, the supernatant was collected and the concentration of Ag^+ in the supernatant was analyzed via inductively coupled plasma–optical emission spectrometry (ICP-OES; PE Optima 8300, PerkinElmer, USA).

2.8. ROS-scavenging capacity of the coatings

2.8.1. DPPH free radical scavenging capacity

Four milliliters of 100 μM 2,2-diphenyl-1-picrylhydrazyl (DPPH) solution in absolute ethanol was added to co-mix with the coated PA film. After incubation in the dark for 1 min, the absorbance of the solution at 517 nm (A_s) was measured using a UV–vis spectrophotometer (Shimadzu UV-2550). The untreated DPPH solution was used as the control group and the absorbance (A_c) was detected. DPPH scavenging was calculated using the following equation:

$$\text{DPPH scavenging (\%)} = \frac{A_s - A_c}{A_c} \times 100\%$$

2.8.2. ABTS free radical scavenging capacity

Four milliliters of 100 μM 2,2'-azino-bis-3-ethylbenzothiazoline-6-sulfonic acid (ABTS) solution in deionized water was added to co-mix with the coated PA film. After incubation in the dark for 5 min, the absorbance of the solution at 734 nm (A_s) was measured using a UV–vis spectrophotometer (Shimadzu UV-2550). The untreated ABTS solution was used as a control and the absorbance (A_c) was detected. We calculated the ABTS removal using the following equation:

$$\text{ABTS scavenging (\%)} = \frac{A_s - A_c}{A_c} \times 100\%$$

2.8.3. In vitro H_2O_2 scavenging capacity

The H_2O_2 scavenging abilities of the coating were evaluated using an H_2O_2 assay kit. In brief, we prepared 4 mL of H_2O_2 solution with a concentration of 1 mmol/L. The H_2O_2 solution was added to each group of samples. All solutions were placed at 37 °C. At specific time points (1, 2, 3, 4, and 5 min), the H_2O_2 concentrations of the solutions were detected as described previously [68].

2.8.4. In vitro ROS-scavenging capacity

The cellular ROS-scavenging ability was investigated. Human umbilical vein endothelial cells (HUVEC) cells (5×10^4 cells/well) were seeded in 24-well plates and incubated at 37 °C for 12 h. The different groups were added and co-incubated with the cells for 24 h. The Rosup reagent (10 $\mu\text{g}/\text{mL}$) was regarded as a positive control and was incubated with the HUVEC cells for an additional 4 h. After washing twice with sterile PBS (pH = 7.4), 2,7-dichlorodihydrofluorescein diacetate (DCFH-DA) solution was added and incubated in the dark for 40 min. Then the cells in the 24-well plates were observed and photographed with an inverted fluorescence microscope (Olympus CKX41, Tokyo, Japan).

2.9. In vitro cytotoxicity evaluation

2.9.1. Cell counting kit 8 (CCK-8) assay

The CCK-8 assay was used to assess the cytotoxicity of the coating on HUVEC and L929 cells. Briefly, HUVEC and L929 cells were seeded in 24-well plates (5×10^4 cells/well), the coated PA films were added, and the samples were incubated with the cells for 24 h and 72 h, respectively. After incubation, the samples were carefully removed from the 24-well plates with forceps and the CCK-8 assay was performed according to the manufacturer's protocol. Uncoated PA film cultured with the cells was used as the control group, and the CCK-8 kit treated solution was transferred to the 96-well plate. The absorbance of the final solution was recorded at 450 nm using a microplate reader (Bio-Tek, USA) to obtain the absorbance.

2.9.2. Live/dead staining assay

The live/dead cell staining kit was used to indicate cellular growth after co-mixing with the coating. HUVEC and L929 cells were manipulated using the above experimental procedure. After removing the material and rinsing the cells with PBS, 300 μL CalceinAM/PI Live/Dead staining solution was added and incubated for 20 min, and the cells were observed using an inverted fluorescent microscope (Olympus CKX41, Tokyo, Japan). The live and dead cells were stained with green and red fluorescence, respectively.

2.9.3. Ki-67 immunofluorescence cell staining

L929 cells were seeded at 5×10^4 cells into a 24-well plate, and different groups of samples were added to the plate for incubation. At 24 h and 72 h, the medium was removed and 200 μL of 4 % Paraformaldehyde (PFA) was added to each well for 30 min at room temperature and then rinsed with PBS. Next, the cells were treated with 0.5 % Triton X-100 for 10 min and blocked in 5 % bovine serum albumin (BSA) for 2 h at room temperature. Next, the sections were incubated with rabbit monoclonal Ki-67 antibody (#11882) (1:400 dilution; Cell Signaling Technology, USA) overnight at 4 °C. After washing with PBS twice, the sections were incubated with goat anti-rabbit IgG secondary antibody (A23220) (1:400 dilution; Abbkine, USA) for 1 h at room temperature in the dark. The sections were stained with DAPI solution (Solarbio; China) and incubated at 4 °C for 10 min in the dark. An inverted fluorescent microscope (Olympus CKX41, Tokyo, Japan) was used to observe the Ki67-positive cells which indicated the viability of proliferating cells.

2.10. 16S rRNA gene sequencing and analysis of human scalp

2.10.1. Sample collection

Patients shaved their hair short before collecting their scalp skin samples. This was followed by 30–40 swipes with a sterile cotton swab over a fixed area of the patient's scalp (approximately 10 cm^2) to collect as many skin microbiota as possible in the area. The swabs were then frozen and stored at -80 °C following collection. Bacterial DNA was extracted from cotton swabs as described [69].

2.10.2. Sequencing and analysis

Amplification of the 16S rRNA gene V1-V3 region was performed as described previously, using the Illumina MiSeq 2500 platform (Illumina, USA) with 300 bp paired-end 'V3' chemistry. Sequences were pre-processed and quality filtered before analysis, including size filtering to 460–600 nucleotides. HmmUFOtu was used for sequence alignment and phylogeny-based OTU clustering as described previously. Statistical analysis and visualization were performed using the phyloseq package in the R statistical computing environment.

2.11. Evaluation of antibacterial capacity

2.11.1. Incubation of bacteria

The antibacterial test was performed with *S. aureus* (ATCC 6538), *E. coli* (ATCC 8739), and *P. aeruginosa* (ATCC 15442) received from the Guangdong Institute Of Microbiology. Tryptic soy broth (TSB) (Solarbio, China) and Luria Broth (LB) (Solarbio, China) were sterilized, and the three bacterial strains were cultivated in the corresponding broth at 37 °C with shaking on a constant temperature shaking incubator at 150 rpm overnight.

2.11.2. Bacterial inhibition ratio

Briefly, the coated disks (diameter = 1.5 cm) were placed in the bottom of a 24-well plate, and the uncoated PA disk was used as the control group. The blank group contained pure bacterial suspension. Next, 500 µL of diluted bacterial suspension (10^6 colony-forming units (CFUs) /mL) was added to each well and incubated with the samples at 37 °C for 24 h. The bacterial suspensions were transferred to a 96-well plate and the absorbance was analyzed using a microplate reader (Bio-Tek, USA). The bacterial inhibition ratio was calculated using the following equation:

$$\text{Bacterial inhibition ratio (\%)} = 100 \times \frac{A_p - A_n}{A_p}$$

where A_p is the absorbance of the blank group (pure bacterial suspension after 24 h of culture) and A_n refers to the absorbance of the other groups after 24 h of culture.

2.11.3. Spread plate assay

The bacterial suspension was prepared as described in 2.11.1. After 24 h of incubation with different samples, a small amount of the bacterial suspension was aspirated and diluted with PBS to the appropriate concentration, and 50 µL of the diluted solution was evenly spread on the agar plate (TSA agar plate for *S. aureus* and *E. coli*; LB agar plate for *P. aeruginosa*). Next, the agar plate was placed in a 37 °C incubator for 18–20 h and bacterial colonies were counted using the ImageJ (National Institutes of Health, USA) cell counter.

To test the antibacterial ability of the coating after long-term release, the coated PA disks were placed in a sterile PBS solution for release, and the PBS-containing bottle was placed in a shaking incubator and shaken at 150 rpm. The PA disks were separately removed at 3 and 6 weeks, and tested according to the steps described in the spread plate assay, followed by counting and quantifying the number of colonies of *S. aureus* on TSA agar plates.

2.11.4. Live/dead bacterial staining

The bacterial culture was performed as described in 2.11.1. After the samples were co-mixed with the bacteria for 24 h, the bacterial suspension was aspirated from a 24-well plate, and the surface of the coating was gently rinsed twice with sterile PBS buffer to wash away the planktonic bacteria. The Acridine Orange (AO)/Propidium Iodide (PI) Live/dead staining solution (500 µL) was subsequently added and incubated for 20 min in the dark, followed by observation using an inverted fluorescence microscope (Olympus CKX41, Tokyo, Japan). The live bacteria were stained with green fluorescence and the dead bacteria

were stained with red fluorescence.

2.11.5. Assessment of bacterial morphology

The samples were prepared as described in Section 2.11.4. After rinsing the samples twice with sterile PBS, 300 µL of 2.5 % glutaraldehyde solution was added to each well to fix the bacteria attached to the surface of the coating. Next, the fixation solution was aspirated and subjected to a 50 %, 60 %, 70 %, 80 %, 90 %, 95 %, and 100 % alcohol dehydration series, in that order. Finally, the gold spray treatment was performed with an electron microscope ion sputterer (Ted Pella, USA) for 75 s and the samples were observed under an SEM (Quanta 200, Japan).

2.11.6. Cyclic antibacterial test

The cyclic antimicrobial test is similar to the procedure described in section 2.11.2. After completing a 24 h antimicrobial test, the disks were carefully removed and rinsed briefly with deionized water, after which the sample was ultrasonically cleaned to completely remove residual bacteria attached to the material. Then the samples were used to repeat the next antimicrobial cycle to determine the durability of the composite coatings [70].

2.12. In vivo antibacterial properties of coatings

Balb/c mice used in the experiments were purchased from the Animal Experiment Center of Southern Medical University and were randomly divided into 4 groups (6 mice per group): uncoated PA disks (control group), TA, TA-Ag5, and TAP. All animal experiments were performed according to protocols approved by the Animal Care and Use Committee of Southern Medical University (Guangzhou, China) (Approval number: NFYY-2020-0929).

A subcutaneous infection model was used to verify the antibacterial effect of the composite coating in vivo [37,71]. The mice were anesthetized by the injection of 1 % pentobarbital sodium, and an incision was made on the side of the thigh. The disks were implanted under the skin through the incision, and 100 µL of *S. aureus* suspension (10^7 CFUs/mL) was inoculated subcutaneously. The skin incision was sutured, and the mice were sacrificed in 7 days the skin tissue surrounding the implant was analyzed by staining with hematoxylin and eosin (H & E) to characterize the infection. Further, a sterile cotton swab was used to take the skin sample around the implanted disk to spread onto the agar plate to assess subcutaneous infection.

2.13. Evaluation of in vivo biocompatibility

2.13.1. Subcutaneous implantation of artificial hair coating

Coated artificial hair fibers were subcutaneously buried in balb/c mice, and the skin tissue containing the artificial hair fiber was harvested after 1 week, 2 weeks, 4 weeks, and 12 weeks. The cross-sections of the artificial hair fibers were cut and stained with H & E and immunofluorescence F4/80 staining of macrophages was performed to determine the inflammatory response induced by the artificial hair fiber at different time points [72].

2.13.2. Real-time quantitative PCR

To analyze the levels of inflammatory factors around the implant, the coated disks were embedded in balb/c mice in the dorsal subcutaneous position. After 4 days, 1 week, and 2 weeks, the capsule of the surrounding foreign body reaction caused by the implant was excised. The expression of pro-inflammatory cytokines (TNF- α , IL-10, and IL-1 β) and pro-healing cytokines (TGF- β and IL-6) in the tissues was investigated via qRT-PCR.

2.14. Artificial hair implant model

We constructed an artificial hair implant animal model by

implanting artificial hair fibers with a modified antibacterial coating onto the scalp of Sprague-Dawley (SD) rats. The rats in the experiment were purchased by the Animal Experiment Center of Southern Medical University. First, we fixed the anesthetized rat limbs on the animal table in a prone position. The hair on top of the rat's head was removed. Next, the skin of the scalp area was disinfected with 0.3 % iodophor and 75 % ethanol solution, and a sterile surgical towel sheet was placed around the head of the rats. With the hair transplant punch in hand, the knotted loop at the end of the artificial hair fiber was hooked onto the head of the punch and we punched the rat's scalp at an appropriate angle ($45\text{--}60^\circ$) to a depth of $\sim 4\text{--}6$ mm. The rat's scalp was slowly withdrawn from the perforator, and the artificial hair fibers were implanted onto the rat's scalp.

2.15. Statistical analysis

The data were analyzed using Graphpad prism 8.0 (GraphPad Software, USA). Statistical significance between two and multiple data groups was determined by *t*-test, one-way analysis of variance (ANOVA), and other statistical methods. All statistical quantitative results were expressed as mean \pm standard deviation (SD). The subcutaneous infection experiment included six replicates ($n = 6$) and the other experiment had three replicates ($n = 3$). Statistics were considered significant at $p < 0.05$ (*).

3. Results and discussion

3.1. Polyamide modification

Mussel-inspired and tannin-inspired surface modification strategies endow inert substrate surfaces with abundant and active phenolic hydroxyl groups [17]. As shown in Fig. 1, the fabrication of antibacterial coating on PA substrates was conveniently achieved via multicycle assembly of TA and Ag^+ , and then chemical shielded with a POM

biodegradable polymer. During the deposition process, free Ag^+ could be rapidly reduced to AgNPs in situ due to the presence of abundant reductive phenolic hydroxyl groups of TA. And the scanning electron microscopy (SEM) images show that the obtained AgNPs were between 400 and 800 nm. Interestingly, the AgNPs densities on the PA substrate show an increase with the increase of deposition cycles. The PA surface became increasingly rougher after the deposition of TA-AgNPs-based MPNs for several cycles and became smoother after the surface was coated with POM polymer. This morphological change can also be confirmed by SEM images (Fig. 2A). Similarly, EDS results show that the Ag content in the TA-Ag(n) ($n = 1, 3, 5$) coating increased with the number of cycles, whereas the TA-AgNPs-POM (TAP) showed a decrease in the detected Ag content due to the blocking effect of the POM polymer (Fig. 2B). The mapping images show that the distribution of AgNPs on TAP was uniform, indicating the homogeneous deposition of AgNPs (Fig. 2C).

After the successful deposition of the TAP coating on PA films, we attempted to deposit the TAP coating on the surface of artificial hair fibers which were also made of medical PA. The morphologies of natural human hair as well as uncoated and TAP coated artificial hair fibers were observed by SEM. The SEM results show that TA-Ag5 and TAP coatings were successfully deposited on the surface of artificial hair fibers, and Ag element was uniformly distributed on the surface of TAP-coated artificial hair fibers (Fig. 2D). The surface roughness and morphologies of TA-Ag(n) ($n = 1, 3, 5$) and TAP coatings were further investigated by AFM. As shown in Fig. 3A, the results were similar to those of the SEM images, the surface of the PA film turned rougher after modification with the TA-Ag(n) deposition, which was also observed in the 3D AFM images. The root-mean-squared roughness (Rq) increased from 233.8 to 307.9 nm with the increase of deposition cycle numbers from 1 to 5. When the POM polymer was further chemically coated by POM prepolymer solution dipping and thermal crosslinking, the overall Rq of the coating was decreased to 267.0 nm, and the average height of the coating increased to 61.3 nm (Fig. 3B and 3C). The roughness and

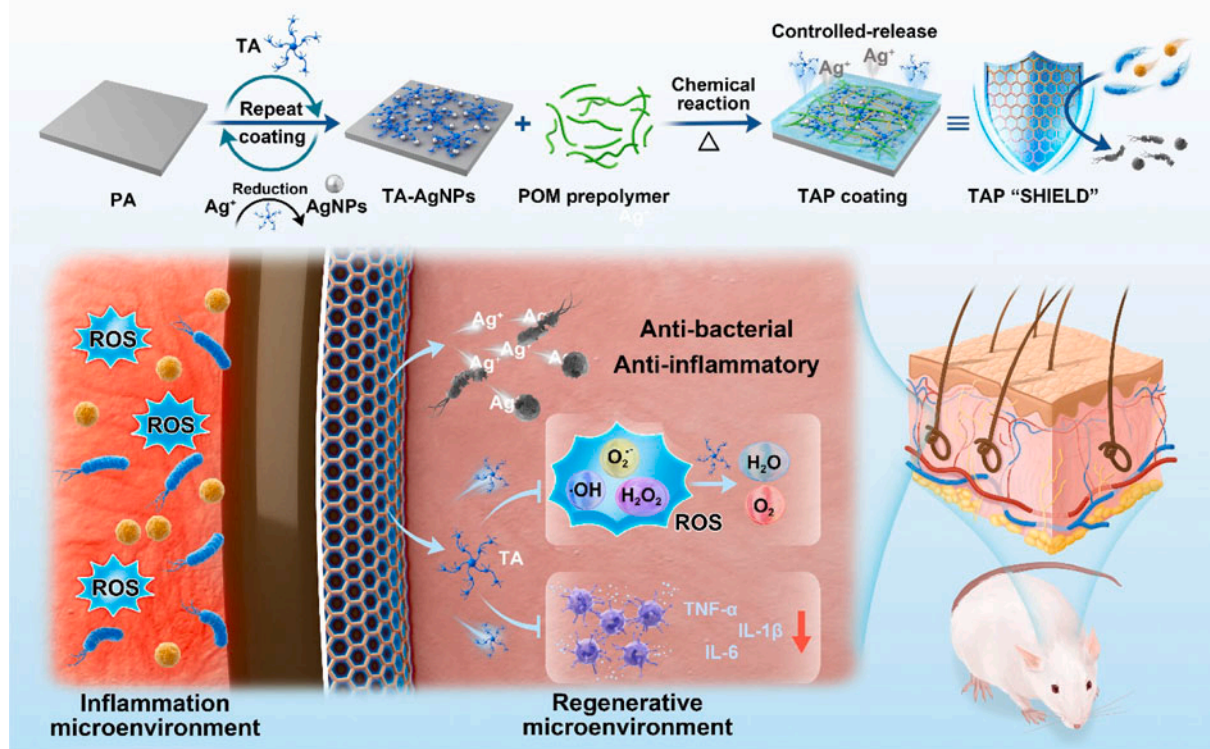


Fig. 1. The schematic illustration of the fabrication process of TAP coating and how its antibacterial and anti-inflammatory properties facilitate its application in the infection prevention and long-term implantation of artificial hair fiber.

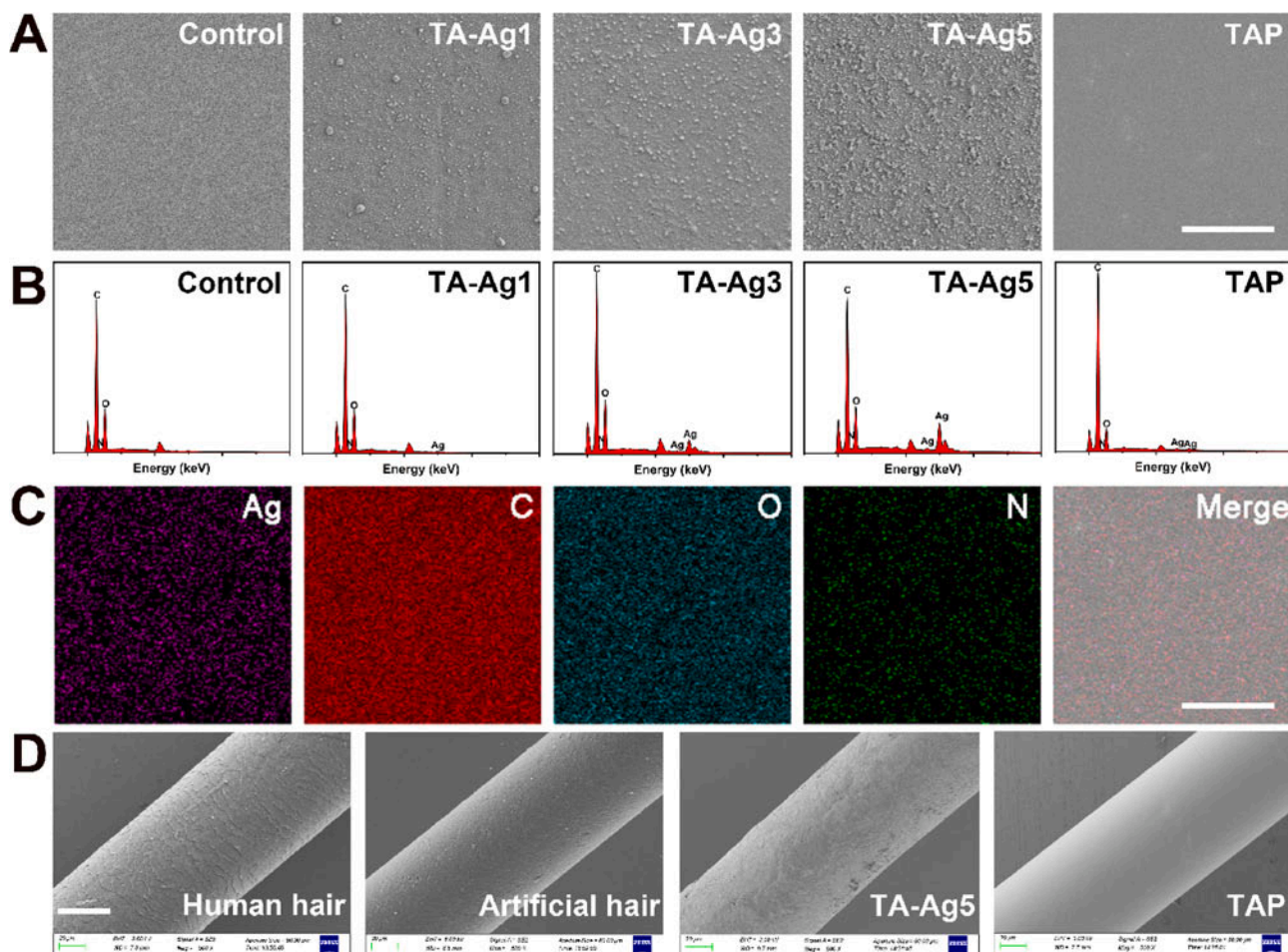


Fig. 2. A) SEM images of un coated (Control) and coated polyamide films (scale bar = 2 μm); B) EDS spectra of control, TA-Ag(n), and TAP samples; C) the mapping images of TAP coated PA film (scale bar = 2 μm); D) the SEM images of natural human hair, polyamide artificial hair and polyamide artificial hair fibers coated with TA-Ag5 and TAP (scale bar = 40 μm).

morphology data of AFM well agree with the previous SEM images. As shown in Fig. 4A, the FTIR spectrum of TAP displays characteristic peaks of $\sim 2930\text{ cm}^{-1}$, which is attributed to the OH stretch. The strong bands at $\sim 710, 1621, 1230,$ and 765 cm^{-1} are attributable to C=O stretching, C=C stretching, C–O stretching, and C=C bending, respectively. We can see that the FTIR of the TAP group has the common characteristic peaks of the other three groups (TA, TA-Ag, POM), indicating the successful deposition of TA-Ag-based MPNs and their further covalent crosslinking with POM polyester on the PA surface. Besides, the surface of uncoated PA showed modest hydrophobicity, whereas the other groups showed good hydrophilicity. In particular, TAP has a water contact angle of 56.6° , and a certain degree of hydrophilicity is beneficial to the adhesion of tissues and cells to the implant surface (Fig. 4B). Next, the detailed chemical compositions of the coated PA films were further analyzed by XPS. From the XPS results shown in Fig. 4C, it can be observed that comparing with TA-Ag(n) ($n = 1, 3, 5$), the characteristic peaks for silver (Ag 3d) at 369.1 and 366.3 eV nearly disappeared in the XPS spectrum of TAP, indicating the successful chemical shielding of the deposited TA-AgNPs with POM polymer. Silver possesses an efficient and powerful antibacterial ability but also shows biological toxicity and side effects. Therefore, it is necessary to control the release of Ag^+ in the implanted microenvironment to reduce tissue toxicity while retaining its antibacterial effect. To investigate the controlled-release capacity of the TAP coating, a 60 day Ag^+ release was evaluated by ICP-OES. As shown in Fig. 4D, all groups experienced burst release within the first 24 h. Then the TA-Ag(n) ($n = 1, 3, 5$) groups showed a continue fast release until the show up of a plateau after 7–21

days when all the Ag^+ was exhausted and no longer released. At day 28, the accumulative concentrations of Ag^+ for the TA-Ag(n) ($n = 1, 3, 5$) groups were 12.13 ppm, 17.98 ppm, and 26.13 ppm, respectively, st twice of that of the other groups. Longer antimicrobial duration facilitates early trauma repair by reducing the risk of microbial infection.

3.2. *In vitro* ROS-scavenging capacity of the coating

ROS plays an essential role in regulating various physiological functions of living organisms [44]. Similar to wound healing, localized massive ROS presents immediately after the material implantation [45,46]. Excessive ROS can generate oxidative stress around implants, severely limiting their biomedical applications, and having negative effects on the surrounding tissues [47]. The ROS scavenging ability of the modified PA films was investigated *in vitro* using DPPH, ABTS radicals and H_2O_2 scavenging models. Due to the abundance of phenolic hydroxyl groups on the TA molecule, TA can provide enough electrons to reduce the DPPH and ABTS radicals (Fig. 5A, 5B). This study aimed to perform *in situ* reduction and anchoring of silver nanoparticles TA greatly improved the scavenging capacity of the DPPH and ABTS radicals, and the UV–vis spectrum showed a corresponding decrease in the characteristic absorption peak at 517 nm and 734 nm, respectively (Fig. 5C, 5D). However, with the addition of Ag^+ , some of the electrons of the phenolic hydroxyl groups were used to reduce Ag^+ to AgNPs, resulting in reduced antioxidant capacity. The antioxidant capacity of the coatings can be re-enhanced by increasing the deposition cycles of TA-Ag MPNs. Fig. 5E and 5F show that after the chemical shield coating

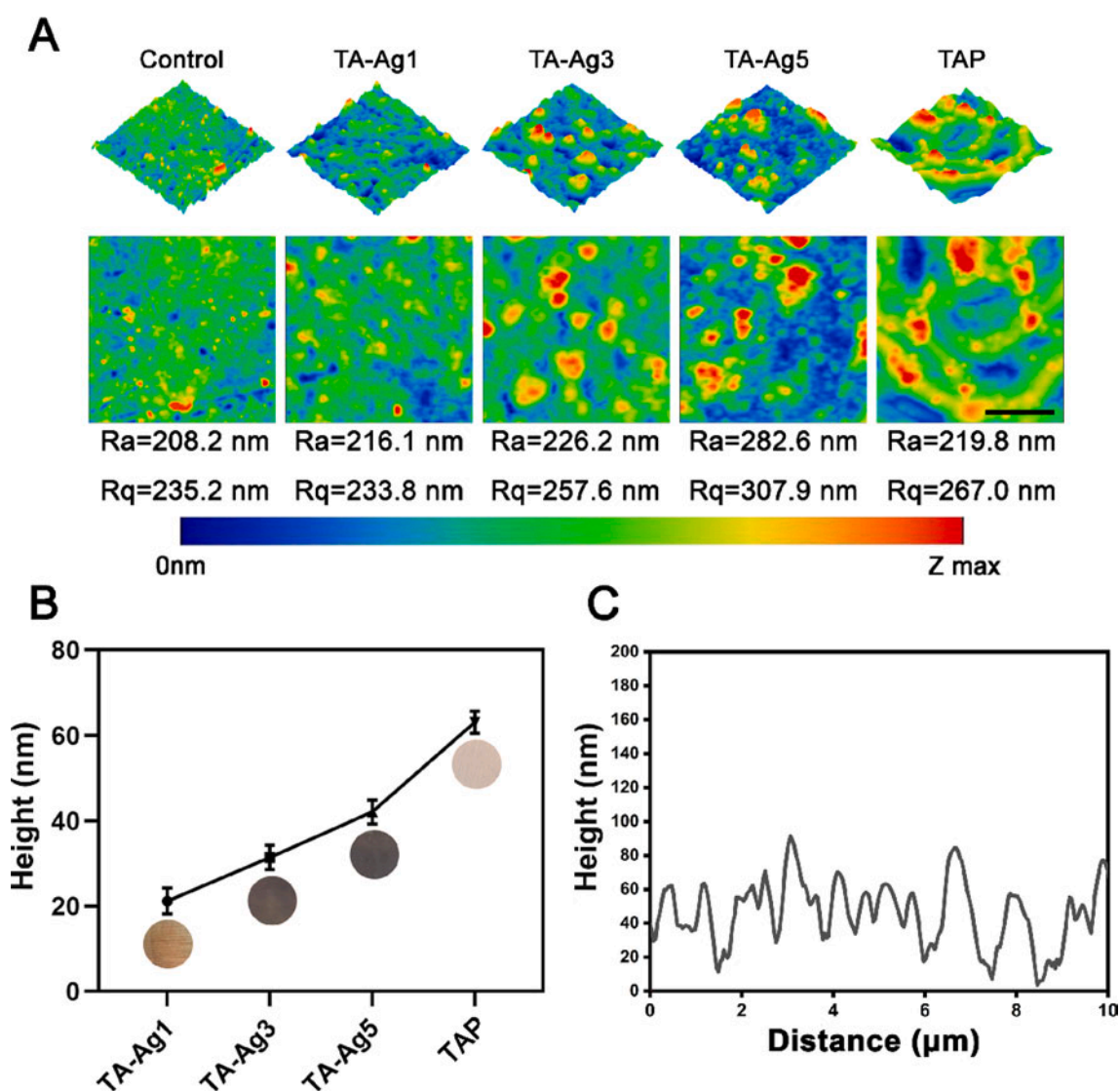


Fig. 3. A) AFM images of polyamide disks without and with TA-Ag(n) and TAP coating (scale bar = 500 nm); B) the photos and heights calculated from AFM images of TA-Ag(n) and TAP coated PA disks; C) the average heights of TAP coating obtained by AFM.

of POM polymer, the antioxidant capacity of TAP is lower than that of TA-Ag5, especially in the case of ABTS scavenging percentage. Additionally, TA also improved the capacity of the coatings to remove free radical H_2O_2 (Fig. 5G). However, the overall antioxidant capacity of the TAP sample is similar to that of TA-Ag3 and still showed good antioxidant efficiency. The antioxidant capacity of the coatings was further confirmed by the intracellular ROS scavenging experiments using HUVECs. The Rosup reagent was used to induce excessive ROS production in the cells and served as a positive control. 2',7'-dichlorodihydrofluorescein-diacetate (DCFH-DA) is a ROS probe showing green colored fluorescence when it is oxidized by intracellular ROS. As shown in Fig. 5H, the fluorescence intensity of the TA and Rosup groups was the lowest and highest, respectively, while the TAP group also showed a good intracellular ROS scavenging ability. Taken together, the results in antioxidant aspects suggest that the inclusion of TA in TA-Ag(n) (n = 1, 3, 5) and TAP coatings conferred them with favorable antioxidant ability.

3.3. In vitro cellular viability and proliferation

Materials used for implants and implantable devices must be biocompatible. Therefore, the viability and proliferation of HUVEC and L929 cells on the coated PA films were evaluated using the cell counting

kit 8 (CCK-8), Live/Dead staining assay, and Ki-67 fluorescent staining assay. In the CCK-8 experiments, incubation of HUVEC and L929 cells on all different samples for 24 h all resulted in no significant difference in absorbance values. At 72 h, due to excessive accumulation of Ag^+ , the absorbance values of the TA-Ag5 groups were reduced modestly compared with other groups in both HUVEC and L929 cells (Fig. 6B and 6D). However, there was no significant difference between the TAP group and the control group, indicating that the chemical shielding of POM polyester had a positive effect on improving the cytocompatibility of the coating. As the outermost layer of the TAP coating, POM may serve as a roadblock to reduce the release rate of Ag^+ into the tissue regenerative microenvironment.

A similar trend was observed in the Live/Dead staining analysis, where the number of alive cells with green fluorescence showed no significant difference between the groups at 24 h and 72 h. However, at 72 h, more dead cells with red fluorescence appeared in the TA-Ag5 group, whereas there was no significant difference between the results of the TAP group and the control group (pure PA film) (Fig. 6A and 6C). Based on the above results, we hypothesize that along with the increase of deposition cycles of TA-AgNPs, the amount of TA and Ag^+ released by the coating to the system increased. And excess silver ions have been reported to affect cellular activity through several potential pathways,

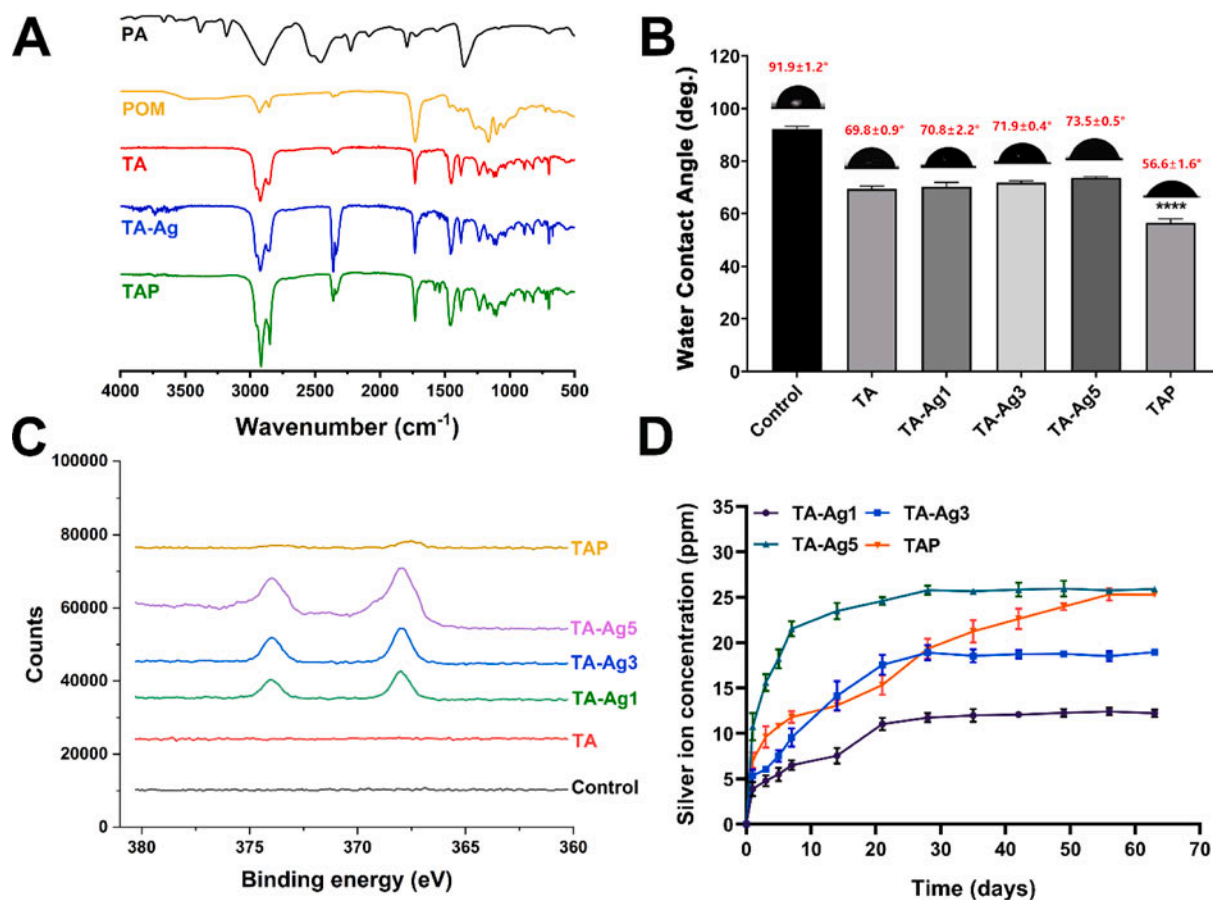


Fig. 4. A) FTIR spectra, B) water contact angle, and C) XPS spectra of polyamide disks without and with TA-Ag(n) and TAP coating; D) the release curves of Ag⁺ from the TA-Ag(n) and TAP coating in PBS at different time points. **** $p < 0.0001$.

including induction of intracellular oxidative stress, disruption of cell membrane integrity, and damage to cellular DNA and leading to apoptosis [24,48,49]. This may have a modest side effect on cell proliferation, which may explain the relatively low absorbance value and the modest increase in the number of dead cells in the TA-Ag5 group. However, the results of CCK-8 and Live/Dead staining of the TA-Ag5 group showed that most of the cells still retained good cellular activity, indicating that the cytotoxicity of the TA-Ag5 coated PA film was negligible.

To further understand whether the coating affects cell proliferation, we performed Ki-67 immunofluorescence staining on cells by incubating with the coating samples for 24 h and 72 h. As shown in Fig. 6E, the control group showed the highest Ki-67 positive ratio, with 23.4 % and 25.4 % Ki-67⁺ stained cells at 24 h and 72 h, respectively. However, as the PA film was gradually deposited with TA-AgNPs-based MPNs, the number of Ki-67⁺ cells decreased gradually (Fig. 6F). We hypothesized that this phenomenon may be related to the increased content of Ag in the coating. However, the chemical shielding of TA-AgNPs by the POM polyester significantly improved the Ki-67⁺ cell percentage, and the Ki-67⁺ cell percentage of the TAP group (~15 %) was much higher than that in other TA-Ag(n) (n = 1, 3, 5) groups (all < 10 %). There may be two potential reasons behind this phenomenon. On the one hand, the POM polymer slows the release of Ag⁺ and reduces the cytotoxicity of Ag⁺. On the other hand, the biodegradable POM polymer will continuously and slowly release L-malic acid (MA) in the microenvironment thus potentially promoting cell proliferation and growth. The main reason is that MA is an intermediate of the tricarboxylic acid (TCA) cycle, involved in cellular metabolism and the production of energy substances such as ATP, exogenous supplementation of MA may enhance cellular activity and proliferative viability [50–53].

3.4. In vitro antibacterial performance

In medical implants, associated bacterial infections often lead to peri-implantitis, which is a series of inflammatory infections in the tissues surrounding the implant that consequently result in implant failure. There may be several possible reasons for this. First, the implant may not fit the surrounding tissues, making it a potential pathway for microbial invasion. Second, bacteria tend to adhere to the surface of the implant and produce a stubborn biofilm, which makes bacteria resistant to antibiotics and other drugs. As a result, they cannot be eliminated. Third, the weak antimicrobial properties of the implant itself render it unable to resist bacterial adhesion, resulting in a very low threshold of infection. Therefore, the antimicrobial capacity of the implant is significantly important to avoid bacterial colonization and infection. Common pathogens reported in infections following artificial hair implantation are *Staphylococcus*, *Escherichia*, *Pseudomonas*, and other opportunistic pathogenic microorganisms. Herein, we performed 16 s sequencing of scalp microorganisms from 21 clinical patients and found inter-individual variability at genus levels. According to the 16 s sequencing results of human skin microbes reported in previous articles, *Cutibacterium* and *Staphylococcus* are the most common commensal microbes on the surface of human skin [54]. Similarly, as shown in Fig. 7A, *Cutibacterium* and *Staphylococcus* are also the most common genera in our human scalp microbial samples, in addition to *Lawsonella*, *Sediminibacterium*, *Escherichia*, and other microbial genera. In general, the most abundant genera *Cutibacterium*, *Staphylococcus*, and *Sediminibacterium* accounted for approximately 62 %, 17 %, and 6 % of scalp microbes, respectively, and the remaining genera accounted for approximately 15 % (Fig. 7B). It is worth noting that in the past infection cases of artificial hair fiber implantation, in addition to the relatively high proportion of

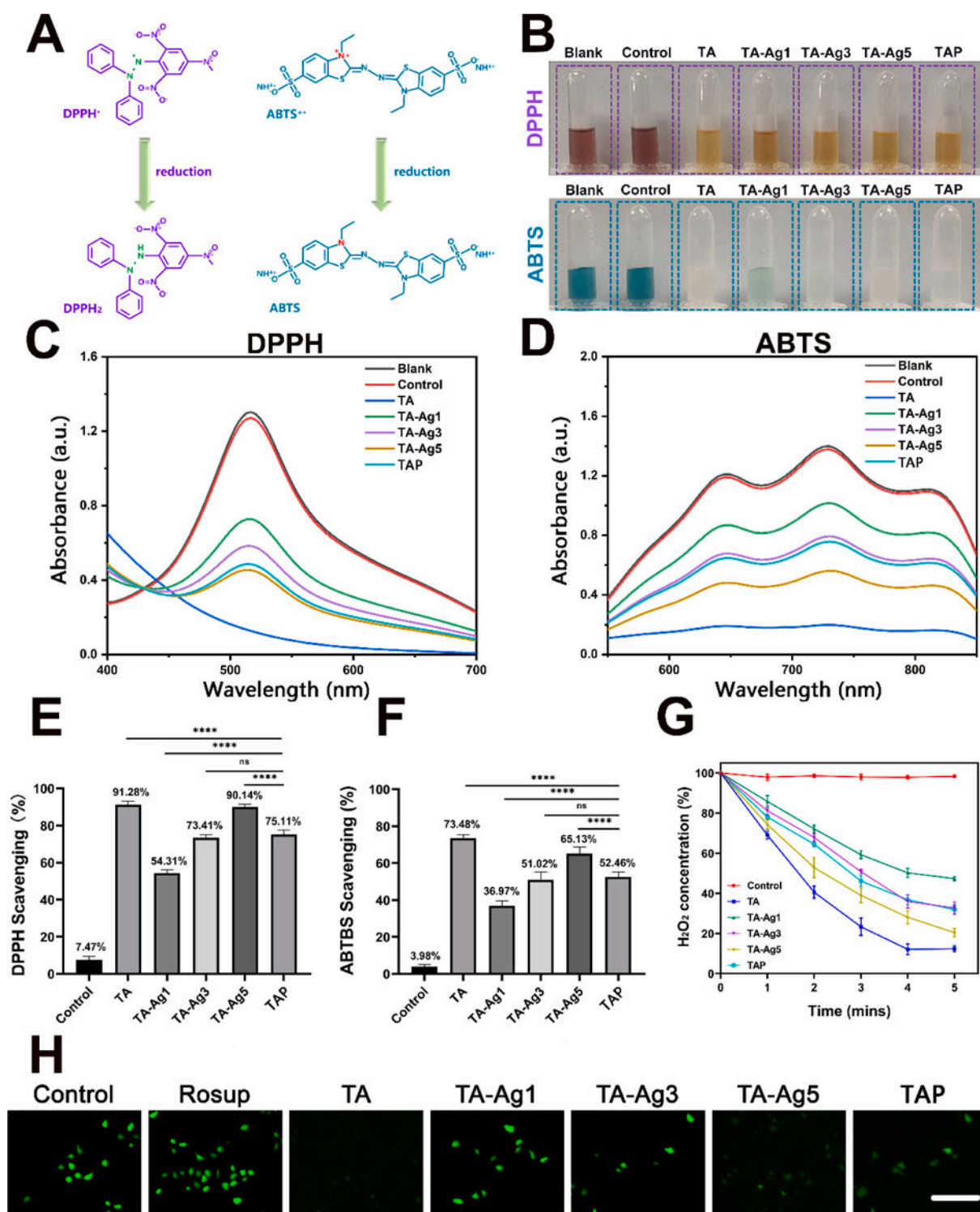


Fig. 5. A) Schematic diagram of the reduction reaction of DPPH and ABTS free radicals; B) photos of DPPH and ABTS solutions reduced by different coatings; UV-vis spectra of C) DPPH solutions and D) ABTS solutions before (Blank) and after being treated with TA-Ag(n) and TAP coated polyamide (PA) disks; E) the DPPH scavenging percentages and F) the ABTS scavenging percentages of TA-Ag(n) and TAP coated PA disks; G) remained H₂O₂ concentrations after being treatment with TA, TA-Ag(n) and TAP coated PA disks for different times. H) the fluorescent images of Rosup-stimulated HUVEC cells after being treatment with different coatings (untreated cells were used as the negative control, and cells treated with only Rosup were used as the positive control) (scale bar = 50 μm). *****p* < 0.0001, ns means no statistically significant difference.

Staphylococcus, *Escherichia* and *Pseudomonas* have also been reported as the most common pathogens [55,56]. Compared with other skin commensal microorganisms, they are more likely to cause opportunistic infections after implantation, which may be due to their stronger virulence, the release of toxin factors, and the formation of more stubborn

biofilms [57,58]. Combining previous reports of artificial hair infection cases and the results of 16S sequencing of human scalp bacteria, *Staphylococcus aureus* (*S. aureus*), *Escherichia coli* (*E. coli*), and *Pseudomonas aeruginosa* (*P. aeruginosa*) were selected as representative bacteria to test the antimicrobial properties of our coatings.

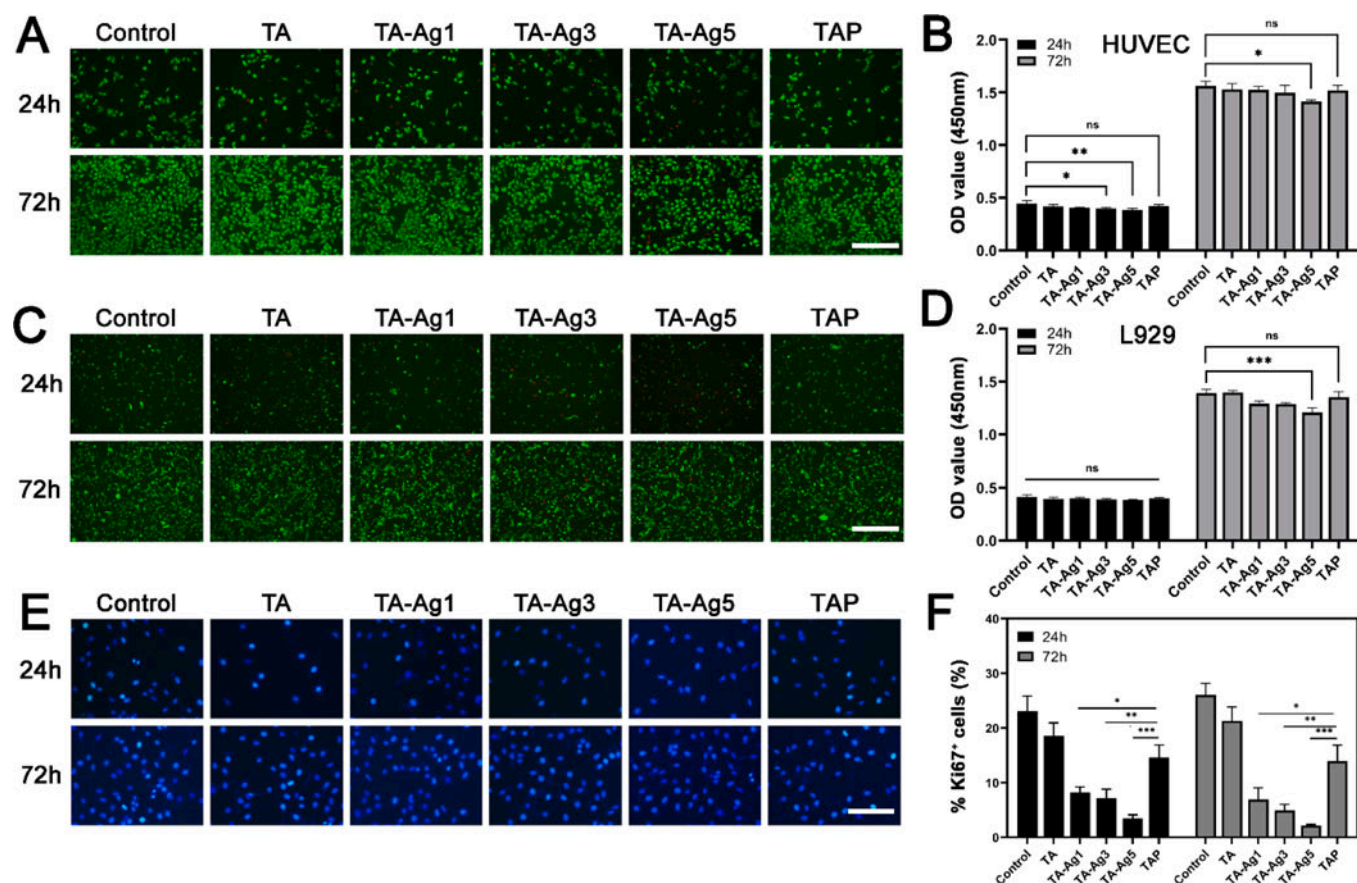


Fig. 6. A) The Live/Dead staining images (scale bar = 100 μ m) and B) CCK-8 OD values of HUVEC cells grown on PA disks uncoated and coated with TA, TA-Ag(n) and TAP for 24 h and 72 h; C) the Live/Dead staining images (scale bar = 100 μ m) and D) CCK-8 OD values of L929 cells grown on PA disks uncoated and coated with TA, TA-Ag(n) and TAP for 24 h and 72 h; E) the Ki67 fluorescence staining (scale bar = 50 μ m) and F) the calculated %Ki67⁺ cell of L929 cells treated with PA disks uncoated and coated with TA, TA-Ag(n) and TAP for 24 h and 72 h. * p < 0.05, ** p < 0.01, *** p < 0.001, ns means no statistically significant difference.

According to the bacterial inhibition ratio assay and results from the spread plate assay, we evaluated the killing ability of the coating against planktonic bacteria. After the bacterial suspension was incubated with the coatings for 24 h, the TA-Ag5 and TAP groups showed the most prominent antimicrobial ability, with a 24 h inhibition ratio of 97.6 %, 94.8 % (*S. aureus*), and 97.3 %, 95.2 % (*E. coli*), and 93.3 %, 94.3 % (*P. aeruginosa*) for both groups for the three bacteria, respectively. Although the chemical shielding by POM polyester may affect the release of Ag⁺, the antibacterial performance of TAP was not significantly affected. The antimicrobial ability of the TA-coated film was weak, whereas the amount of Ag in the TA-Ag1 and TA-Ag3 coatings was not enough to completely kill most of the bacteria (Fig. 8A, 8B and 8C). Next, we diluted the bacterial suspension and spread it on a TSA agar plate. The results were consistent with those for the inhibition ratio results. The control group had the highest number of bacterial colonies relative to other groups, and as the number of TA-AgNPs-based MPNs deposition cycles increased, the antimicrobial capacity increased, and the number of colonies gradually decreased. In general, the TA-Ag5 and TAP groups showed the strongest bacterial killing ability against planktonic bacteria compared to other groups. The results indicated that chemical shielding by POM polymer did not have a significant influence on the short-term antimicrobial ability of the TAP composite coating. Further, the long-term antibacterial ability against *S. aureus* of TAP coating was studied using the 3 weeks and 6 weeks released solutions of the coated PA disks in sterile PBS solution. Compared with the short-term (24 h) antibacterial experiment results, the antibacterial ability of the coating gradually decreases due to the continuous release of Ag⁺. At 3 weeks, the antibacterial ability of all groups decreased to varying degrees due to the depletion of Ag⁺. At this time, TAP exhibited the

strongest antibacterial properties due to the sustained-release effect of the POM encapsulation. As time progressed to 6 weeks, TAP was still able to kill about half of the bacteria, and the other groups were almost indistinguishable from the control group. The results of this experiment were also confirmed by the results of Ag⁺ release because TAP still released Ag⁺ continuously at 3 and 6 weeks, which also confirms the excellent performance of the TAP coating in terms of antibacterial persistence.

The above results show that the TAP coating effectively releases Ag⁺ into the surrounding environment to prevent bacterial infection, and shows antibacterial activity before the planktonic bacteria attach to the implant surface in the short and long term, respectively. However, the implant placement can cause localized damage to the organism. In the early stages of implantation, the barrier function around the implant is weak, and microorganisms and other pathogens may still break through the barrier and adhere to the surrounding environment and its surface. One of the initial prerequisites for the formation of an undesirable bacterial biofilm is the adhesion of bacteria to the implant surface, followed by colonization, aggregation, and secretion of large amounts of extracellular aggregates to form a mature biofilm. This creates conditions for the subsequent spread of infection to the host. Therefore, it is crucial to evaluate the ability of the implant to kill bacteria that adhere to the surface (Fig. 9A). As shown in Fig. 9B, the results of the Confocal Laser Scanning Microscope (CLSM) indicated that TA-Ag5 and TAP killed nearly all the bacteria, with microscope images showing a strong red fluorescence indicating dead bacteria. However, strong green fluorescence from live bacteria was observed in the control groups and TA groups, while the TA-Ag1 and TA-Ag3 groups appeared as red dead bacteria mixed with green live bacteria (Fig. 8B). If the invasive bacteria

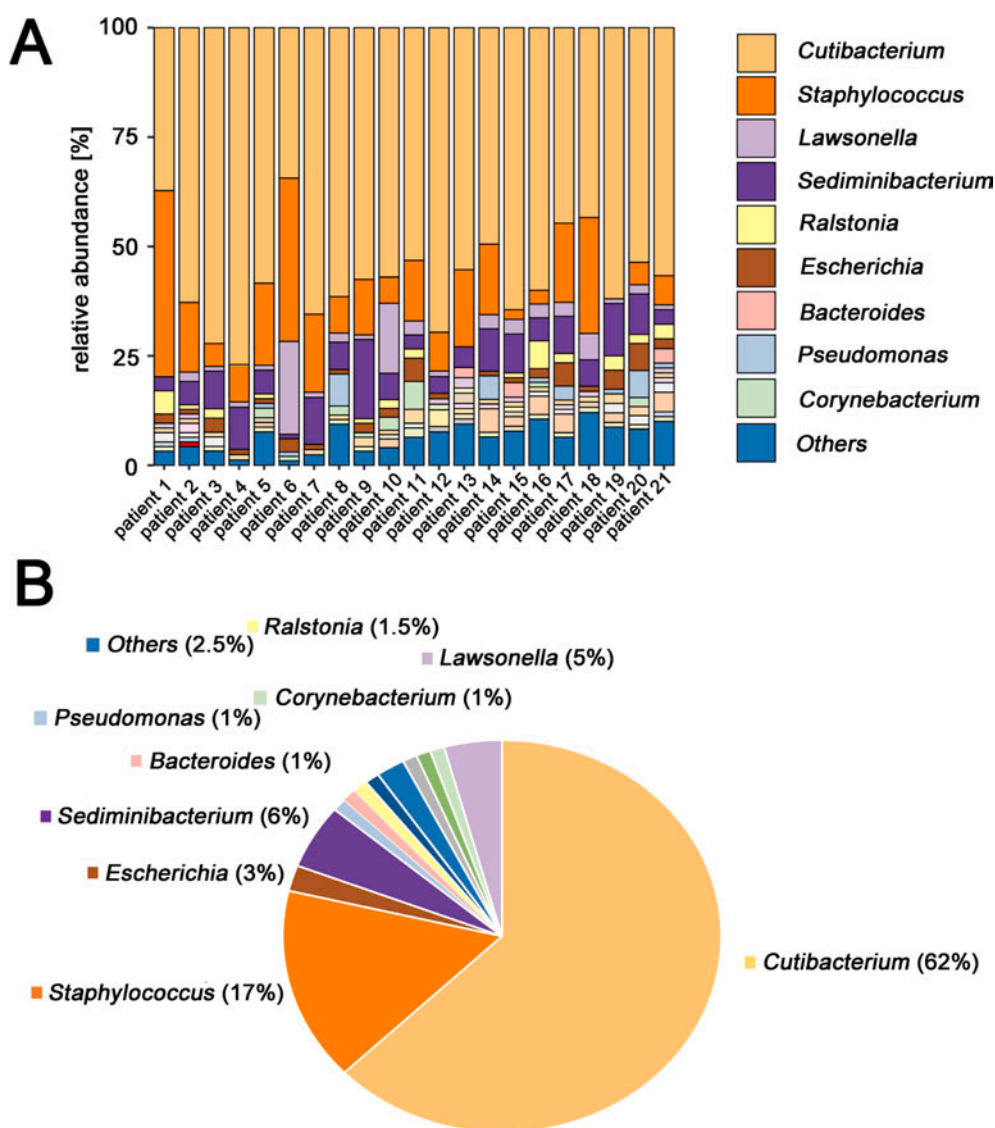


Fig. 7. A) Percentages of taxonomic classifications at genus level of 16S rDNA sequence from skins of 21 patients scalp; B) total percentages of different genus of scalp microbiome in 21 patients.

break through the defensive barrier and attach to the coating surface of TA-Ag(n) ($n = 1, 3, 5$) and TAP, most of the *S. aureus*, *E. coli*, and *P. aeruginosa* would be eliminated. As shown in the bacterial contact killing assay results in Fig. 9C, the addition of silver caused the bacteria on the coating surface to deform and undergo cell death compared to the control and pure TA-modified groups. Overall, the above results show that the TAP coating is effective in killing both planktonic and adherent bacteria, thus preventing the development of peri-implantitis due to bacterial colonization.

3.5. Long-lasting antibacterial property

We investigated the long-term anti-bacterial activities of the TAP composite coating and set a 24 h incubation cycle. The TA-Ag5 coating exhibited the best anti-bacterial activity with an average of > 97 % inhibition ratio for all three bacterial types (*S. aureus*, *E. coli*, and *P. aeruginosa*) in the first cycle. The TAP composite coating also performed well, with an antibacterial efficiency close to 94 % (average 93.97 %). As the number of incubations increased, the antibacterial ability of all groups decreased to varying degrees. Due to the lack of encapsulation by the biodegradable POM polymer, the multicycle-assembled TA-Ag(n) coating could not prevent the rapid release of

antibacterial Ag^+ . Thus, except for the TAP group, the antibacterial efficiency of other groups dropped significantly after the first three cycles. For the third and fifth incubation cycles, the anti-bacterial ratio of the TA-Ag5 group decreased to 60.7 % and 19.08 %, respectively, and TA-Ag5 showed poorer durability compared with 77.4 % and 41.65 % observed with TAP. In other groups, we observed a sharp decline in the antibacterial efficiency during the second and third cycles, but this phenomenon did not occur in the TAP group, and the overall decline in the antibacterial efficiency of TAP was stable. Eventually, in the last cycle, the antibacterial rates of all groups except TAP were 9.45 %, 8.9 %, 8.67 %, and 19.08 %, respectively, which were $\sim 1/4$ and $1/2$ of that of TAP (41.65 %) (Fig. 9D, 9E and 9F). We speculate that MA released from POM degradation might have synergistic antibacterial effect with TA and Ag^+ . Several interesting recent studies have confirmed that as an organic acid, MA possesses considerable antimicrobial properties against *S. aureus*, *E. coli*, *C. perfringens* and *Salmonella* [59–61], its antimicrobial performance is only slightly weaker than that of L-lactic acid. Overall, the combination of the multi-cycle deposition of TA-AgNPs-based MPNs and the chemical shield by POM in the specially designed TAP architecture successfully prolonged the release duration of Ag^+ up to 56 days. This, together with the synergistic antibacterial effect with TA and MA, conferred the TAP coating with favorable short-term

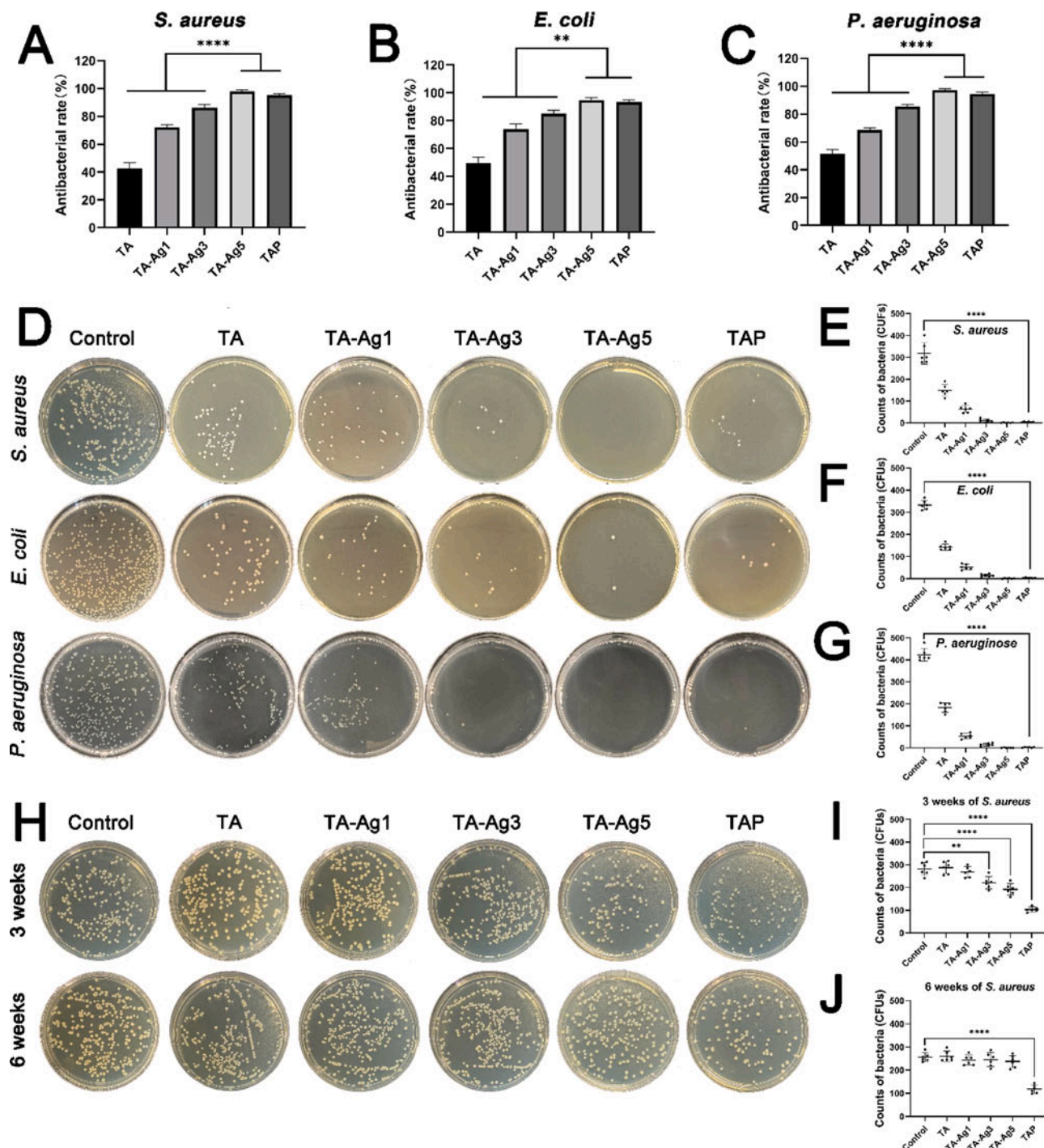


Fig. 8. The 24-hours' antibacterial rates of different samples against A) *S. aureus*, B) *E. coli* and C) *P. aeruginosa* obtained by OD value measurement; D) the images of the grown bacteria colonies on agar plates and the counted colony forming units (CFUs) of E) *S. aureus*, F) *E. coli* and G) *P. aeruginosa* after the bacteria suspensions being treated with uncoated (Control) and coated PA disks for 24 h; H) the images of the grown *S. aureus* colonies on agar plates and I, J) the corresponding quantitative results after the *S. aureus* suspensions being treated with the released solutions of uncoated (Control) and coated PA disks in PBS for 3 and 6 weeks. ** $p < 0.01$, *** $p < 0.001$, **** $p < 0.0001$.

and long-term antimicrobial efficacy, making it possible to prevent bacterial colonization and adhesion, and reduce the incidence of peri-implantitis.

3.6. In vivo anti-infection ability

Based on the infection conditions for several implanted devices, we developed a subcutaneous *S. aureus* infection model to evaluate the

antimicrobial capacity of the coated material (Fig. 10A). Four groups including control groups, TA groups, TA-Ag5 groups, and TAP groups were selected for the next in vivo experiments. Different groups of coated PA disks were embedded subcutaneously on the dorsal side of the Balb/c mice, and a 100 μ L bacterial suspension (10^7 CFUs/ml) was injected for incubation with the coated disks. The surgical site was opened after 7 days, we found that the disks coated with TA-Ag5 and TAP showed a good antimicrobial effect with no infection under the skin

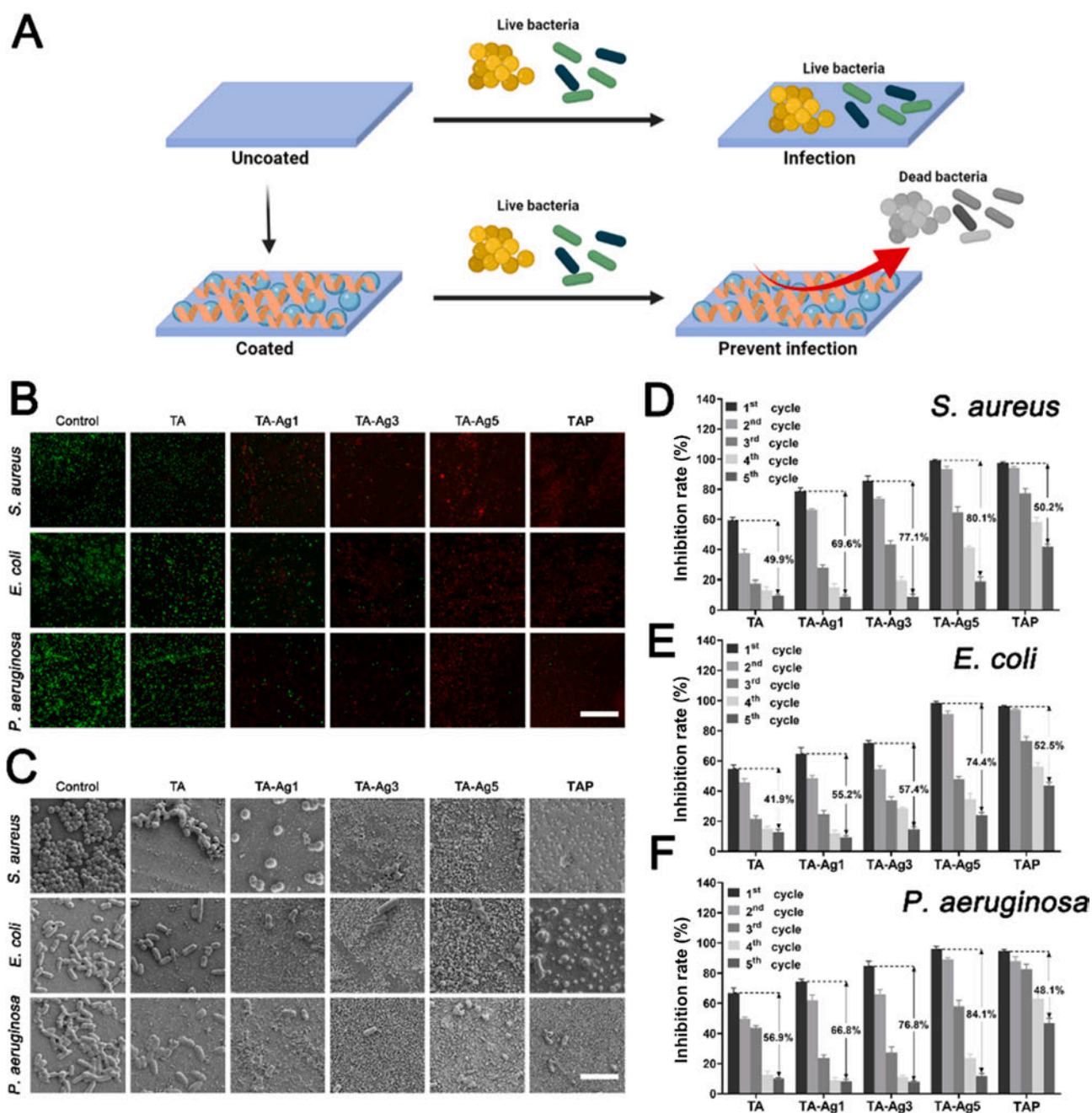


Fig. 9. A) Schematic illustration of antibacterial coating against adhered bacteria; the antibacterial activities reflecting by B) Live/Dead staining images (scale bar = 50 μm) and C) SEM images of uncoated (Control) and coated PA disks against *S. aureus*, *E. coli* and *P. aeruginosa* after 24 h' incubation (scale bar = 10 μm); the cyclic antibacterial inhibition rates of different samples against D) *S. aureus*, E) *E. coli* and F) *P. aeruginosa* (cycle numbers = 1 ~ 5).

of the mice. In contrast, most mice implanted with uncoated disks or pure TA coating developed subcutaneous abscesses and showed severe skin infections (Fig. 10B). These results indicated that the TAP coating had a superior antibacterial capacity consistent with the in vitro results. Further, we scraped the abscess from the surgical site with a sterile cotton swab and spread it onto the TSA agar plate. The agar plates of the control group were covered with *S. aureus* colonies, whereas it was much higher than that of the TA-Ag5 group and the TAP group (Fig. 10B). The skin and muscle tissue around the surgical area was removed for H & E staining to observe the bacterial infection. The H & E images showed that infection in the control group resulted in acute inflammatory cell aggregation, which was rarely observed in the TAP group (Fig. 10B, 10C, and 10D). The above results demonstrated that the TAP coating could effectively inhibit *S. aureus* infection, and possessed excellent

antibacterial performance in vivo.

3.7. In vivo biocompatibility and anti-inflammation

To investigate the biosafety of the coatings, the disks were implanted under the skin of mice, and major organs such as the heart, spleen, liver, lung, and kidney of mice were observed using H & E stained images. No damage or obvious adverse effect was observed in the main organs of mice implanted with the disks (Fig. S1). Implantable medical devices can be recognized as foreign objects by the host immune system, triggering a series of interactions at the implant-host interface, might result in a foreign-body response (FBR), such as a strong inflammatory response, foreign body giant cell formation, fibrosis, requiring the isolation of the medical implants from the host in extreme cases. The

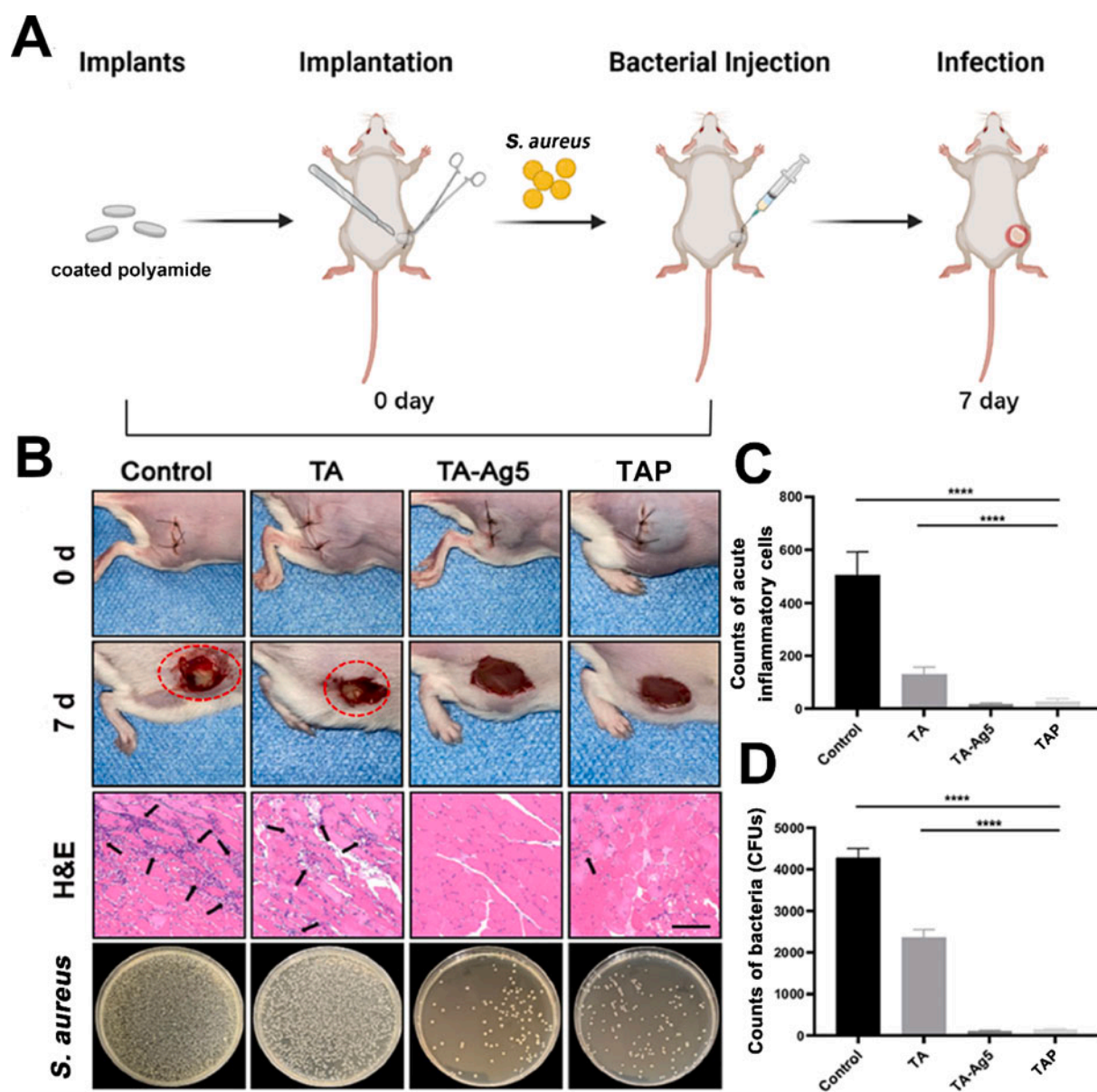


Fig. 10. A) Schematic illustration of the implantation of coated polyamide (PA) disk and the creation of infected mice model by the inoculated of *S. aureus* followed by incubation for 7 days; B) the images of mice implanted with coated and uncoated PA disks on day 0 and day 7 (wounds were cut), the H&E staining images of the tissue slices surrounding the infected sites on day 7 (the blank arrows indicate acute inflammatory cells), and the images of the residual bacteria on day 7 (the subcutaneous abscesses were scraped with a cotton swab and inoculated on TSA agar plates); C) the counts of acute inflammatory cells reflecting the infection levels of subcutaneous tissues; D) the counts of *S. aureus* on agar plates. **** $p < 0.0001$.

strong foreign body reaction of the implant can result in potential interruption of nutrient delivery, tissue deformation, and eventual implant failure. We evaluated the tissues surrounding the coated artificial hair fiber after implantation for 1, 2, 4, and 12 weeks. As shown in the H & E staining images, quantitative inflammatory numbers, F4/80 macrophage immunofluorescence staining images and the corresponding quantitative results in Fig. 11A and 11B, the control and TA-Ag5 groups induced relatively severe inflammatory reaction in the surrounding tissues at week 1 and 2, which was reduced but still existed at week 4 (Fig. S2). The tissues surrounding the implant in the TA and TAP groups showed a significantly decreased inflammatory cells ($p < 0.0001$) and lower density of macrophages ($p < 0.0001$) than that in the control and TA-Ag5 groups at week 1, 2, and 4 post-implantation (Fig. 11A and 11B). As reflected by the H & E staining images, F4/80 macrophage immunofluorescence staining images and the corresponding quantitative results shown in Fig. S2, the acute inflammatory

reaction disappeared at week 12 for all tested groups. These results indicate that the TAP coatings possess superior biocompatibility comparing to the uncoated artificial hair fibers and TA-Ag5 coated ones, guaranteed their potential clinical application.

To further study the anti-inflammatory efficacy of TAP coating, the expression levels of the inflammation-related cytokines (TNF- α , IL-6, IL-1 β , IL-10 and TGF- β) in the harvested tissues surrounding the artificial hair fibers during the first 2 weeks after operation were analyzed via qRT-PCR. As shown in Fig. 11C, at 24 h, for all groups, the expression levels of pro-inflammatory genes including TNF- α , IL-6 and IL-1 β , were high, with the TA-Ag5 group the highest. This may be caused by the locally high concentration of Ag⁺ released by the TA-Ag5 coating. Several studies have reported that silver induces the production of ROS and free radicals thus increased the oxidative stress level, which activates inflammatory signaling cascades leading to elevated inflammatory cytokines such as interleukins and tumor necrosis factor [62,63]. In

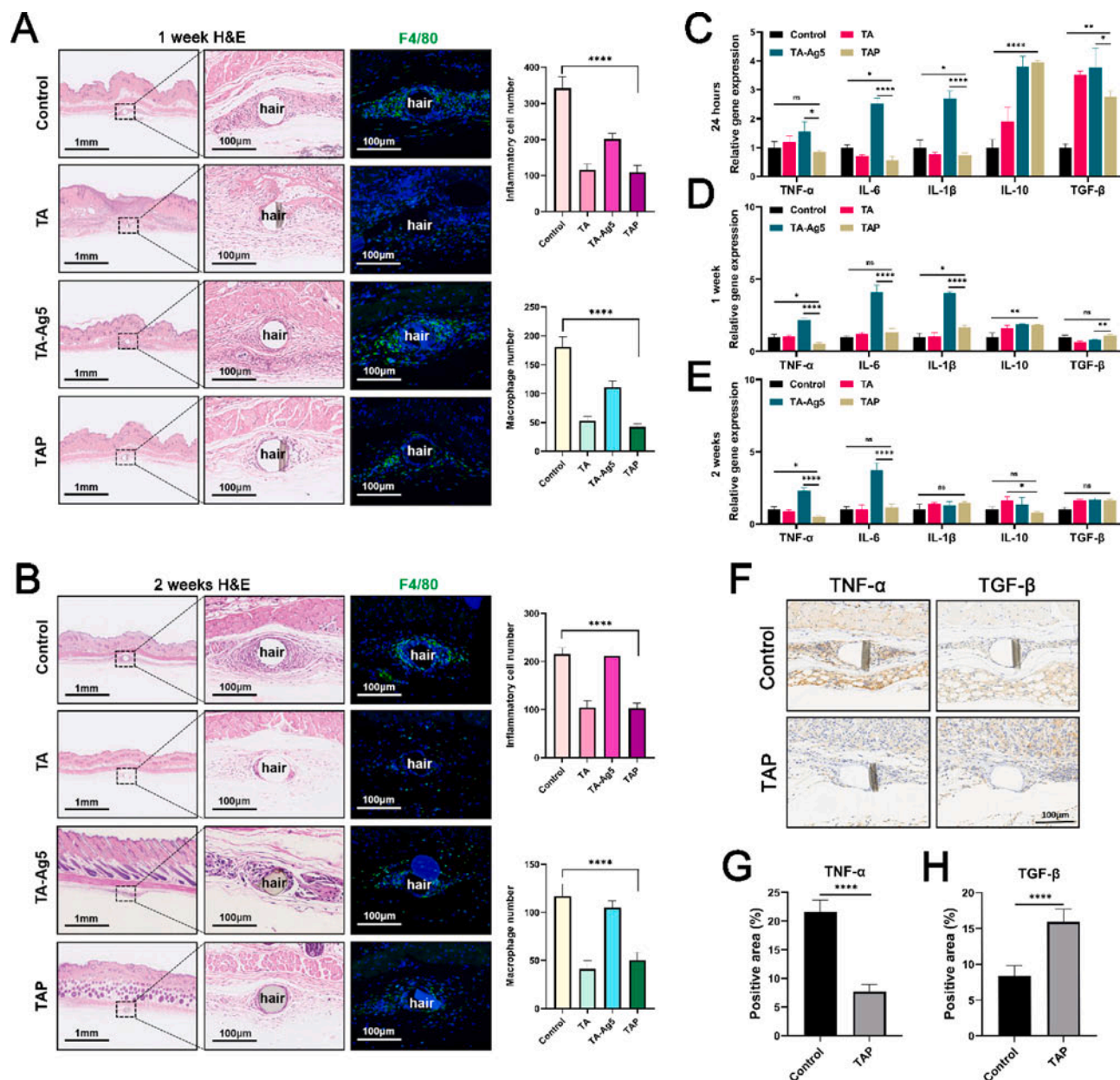


Fig. 11. The H&E and F4/80 (macrophage cells were stained in green) immunofluorescent staining images, and the counted inflammatory cell/macrophage numbers in the tissue slices surrounding the implanted artificial hair fibers at week A) 1 and B) 2; the expression levels of inflammation-related genes (TNF- α , IL-6, IL-1 β , IL-10 and TGF- β) in the tissues surrounding the artificial hair fibers measured by qRT-PCR C) 24 h, D) 1 week and E) 2 weeks after implantation; F) the TNF- α and TGF- β immunohistochemical staining images 3 days after implantation, and the expression levels of G) TNF- α and H) TGF- β of the tissues surrounding the artificial hair fibers. * $p < 0.05$, ** $p < 0.01$, **** $p < 0.0001$, ns means no statistically significant difference.

contrast, the acute inflammatory response of the POM-shielded TAP group was significantly lower than that of the TA-Ag5 group at 24 h (Fig. 11C). At week 1 and 2, the differences in the expression levels of inflammation-related cytokines among the control, TA and TAP groups were no longer significant, but the expression levels of inflammation-related cytokines in the TA-Ag5 group still stayed at high levels (Fig. 11D and 11E). At the same time, the expression levels of anti-inflammatory (IL-10) and pro-healing (TGF- β) cytokines of the TA-Ag5 and TAP groups were the highest in all the tested three time points (Fig. 11C, 11D and 11E), implying that TA-Ag5 and TAP coatings possess the ability to better initiate tissue regeneration immediately after the trauma caused by implantation. Finally, the in vivo inflammatory responses of the TAP group was further studied via TNF- α and TGF- β immunohistochemical staining 4 days after the implantation of unmodified and modified artificial hair (Fig. 11F). As shown in Fig. 11F,

11G and 11H, the expression levels of TNF- α ($p < 0.0001$) and TGF- β ($p < 0.0001$) in the TAP group were significantly lower and higher than that of the control group, respectively. These results proved the superior anti-inflammatory efficacy of TAP coating. In the TAP coating system, the antioxidant and free radical scavenging property [64–66] of tannic acid (TA) make it can well coordinate ROS scavenging and the reduction of the subsequent inflammatory factor signaling induced by trauma and Ag $^+$. At the same time, the role of the inclusion of POM polymer as a chemical shielding layer in improving the level of antioxidative ability of the TAP coating cannot be ignored, as it moderates the release of Ag $^+$ in the microenvironment on the one hand, and L-malic acid released from POM also acts as an antioxidant in concert with TA on the other hand [67]. Overall, these results obtained after implantation at different time points indicated that the TAP coating may serve as a class of promising anti-inflammatory and biocompatible materials.

3.8. Artificial hair fiber implant investigation

To assess the in vivo applicability of TAP coating, TAP-coated artificial hair fibers were carefully implanted into the scalp of rats using surgical instruments to a depth of approximately 4–5 mm. After the artificial hair was implanted onto the rat's scalp, no obvious bleeding, inflammation, or redness was observed (Fig. S3), implying that TAP coating has a good potential for in vivo application as an anti-inflammatory and antibacterial coating for implantable materials.

4. Conclusions

A tannic acid-silver nanoparticles (TA-AgNPs)-based metal-phenolic networks (MPNs)-poly(1,8-octanediol L-malate) (POM) (TAP) coating with long-term antibacterial and anti-inflammatory capacity was developed by reacting TA with Ag⁺ in a multicycle assembly manner to strongly adhere TA-AgNPs-based MPNs onto the polyamide (PA) film surface followed by chemically shielding with POM polymer via a subsequent thermal crosslinking process. In the TAP coating, TA effectively bridged the inorganic and organic phases, and the AgNPs on PA in situ reduced by TA endowed the modified PA film with excellent antimicrobial properties. The addition of the peripheral POM polyester layer further improved the biocompatibility and hydrophilicity of the coating, greatly slowed the release rate of Ag⁺, and extended the antibacterial duration up to nearly 60 days, twice as long as those coatings without the POM layer. In vitro antibacterial and ROS-scavenging experimental results further confirmed the considerable antibacterial and antioxidant properties of the TAP coating. Moreover, the antibacterial activity of TAP composite coating was also well demonstrated in the animal subcutaneous infection model, and histological analyses indicate that the inflammatory response caused by *S. aureus* infection was vastly counterbalanced in the TAP group. Subcutaneous biocompatibility experiments with artificial hair from 1 to 12 weeks demonstrated that the TAP-coated artificial hair fibers evoked a reduced degree of inflammatory response compared to the uncoated group. Thus, the TAP coating might have a great application potential in prolong the implantation duration of artificial hair fibers, and the design strategy for inorganic-organic hybrid composite coating materials can also be expanded to various application scenarios needing the prevention of microbial infection and the maintenance of favorable biocompatibility.

Declaration of Competing Interest

The authors declare that they have no known competing financial interests or personal relationships that could have appeared to influence the work reported in this paper.

Data availability

Data will be made available on request.

Acknowledgements

Funding: This work was supported by the Natural Science Foundation of China [grant numbers: U21A2099, 82272453, 82102545, and 81971889] and the Natural Science Foundation of Guangdong Province [grant number 2019A1515012170].

Appendix A. Supplementary data

Supplementary data to this article can be found online at <https://doi.org/10.1016/j.cej.2022.140572>.

References

- [1] C.R. Arciola, D. Campoccia, L. Montanaro, Implant infections: adhesion, biofilm formation and immune evasion, *Nat. Rev. Microbiol.* 16 (7) (2018) 397–409, <https://doi.org/10.1038/s41579-018-0019-y>.
- [2] M. Cloutier, D. Mantovani, F. Rosei, Antibacterial coatings: challenges, perspectives, and opportunities, *Trends Biotechnol.* 33 (11) (2015) 637–652, <https://doi.org/10.1016/j.tibtech.2015.09.002>.
- [3] Y. Wang, F. Wang, H. Zhang, B. Yu, H. Cong, Y. Shen, Antibacterial material surfaces/interfaces for biomedical applications, *Appl. Mater. Today* 25 (2021), <https://doi.org/10.1016/j.apmt.2021.101192>.
- [4] E. Zhang, X. Zhao, J. Hu, R. Wang, S. Fu, G. Qin, Antibacterial metals and alloys for potential biomedical implants, *Bioact. Mater.* 6 (8) (2021) 2569–2612, <https://doi.org/10.1016/j.bioactmat.2021.01.030>.
- [5] H. Yazdani-Ahmadabadi, D.F. Felix, K. Yu, H.H. Yeh, H.D. Luo, S. Khoddami, L. E. Takeuchi, A. Alzahrani, S. Abbina, Y. Mei, L. Fazli, D. Grecov, D. Lange, J. N. Kizhakkedathu, Durable surfaces from film-forming silver assemblies for long-term zero bacterial adhesion without toxicity, *ACS Cent. Sci.* 8 (5) (2022) 546–561.
- [6] S. Wu, J. Xu, L. Zou, S. Luo, R. Yao, B. Zheng, G. Liang, D. Wu, Y. Li, Long-lasting renewable antibacterial porous polymeric coatings enable titanium biomaterials to prevent and treat peri-implant infection, *Nat. Commun.* 12 (1) (2021) 3303, <https://doi.org/10.1038/s41467-021-23069-0>.
- [7] Y. Wang, Y. Yang, Y. Shi, H. Song, C. Yu, Antibiotic-free antibacterial strategies enabled by nanomaterials: progress and perspectives, *Adv. Mater.* 32 (18) (2020) e1904106.
- [8] C. Zhao, L. Zhou, M. Chiao, W. Yang, Antibacterial hydrogel coating: Strategies in surface chemistry, *Adv. Colloid Interface Sci.* 285 (2020), 102280, <https://doi.org/10.1016/j.cis.2020.102280>.
- [9] D. Şen Karaman, U.K. Ercan, E. Bakay, N. Topaloğlu, J.M. Rosenholm, Evolving Technologies and Strategies for Combating Antibacterial Resistance in the Advent of the Postantibiotic Era, *Adv. Funct. Mater.* 30 (15) (2020), <https://doi.org/10.1002/adfm.201908783>.
- [10] P.P. Kalelkar, M. Riddick, A.J. Garcia, Biomaterial-based delivery of antimicrobial therapies for the treatment of bacterial infections, *Nat. Rev. Mater.* 7 (1) (2022) 39–54, <https://doi.org/10.1038/s41578-021-00362-4>.
- [11] K. Kaniewska, M. Karbarz, E. Katz, Nanocomposite hydrogel films and coatings – Features and applications, *Appl. Mater. Today* 20 (2020), <https://doi.org/10.1016/j.apmt.2020.100776>.
- [12] W. Li, E.S. Thian, M. Wang, Z. Wang, L. Ren, Surface Design for Antibacterial Materials: From Fundamentals to Advanced Strategies, *Adv. Sci. (Weinh)* 8 (19) (2021) e2100368.
- [13] P. Dutta, B. Wang, Zeolite-supported silver as antimicrobial agents, *Coord. Chem. Rev.* 383 (2019) 1–29, <https://doi.org/10.1016/j.ccr.2018.12.014>.
- [14] M. Azizi-Lalabadi, F. Garavand, S.M. Jafari, Incorporation of silver nanoparticles into active antimicrobial nanocomposites: Release behavior, analyzing techniques, applications and safety issues, *Adv. Colloid Interface Sci.* 293 (2021), 102440, <https://doi.org/10.1016/j.cis.2021.102440>.
- [15] C. Cao, N. Yang, Y.e. Zhao, D. Yang, Y. Hu, D. Yang, X. Song, W. Wang, X. Dong, Biodegradable hydrogel with thermo-response and hemostatic effect for photothermal enhanced anti-infective therapy, *Nano Today* 39 (2021), <https://doi.org/10.1016/j.nantod.2021.101165>.
- [16] Y. Wang, B. Cai, D. Ni, Y. Sun, G. Wang, H. Jiang, A novel antibacterial and antifouling nanocomposite coated endotracheal tube to prevent ventilator-associated pneumonia, *J. Nanobiotechnol.* 20 (1) (2022), <https://doi.org/10.1186/s12951-022-01323-x>.
- [17] J. Guo, X. Tian, D. Xie, K. Rahn, E. Gerhard, M.L. Kuzma, D. Zhou, C. Dong, X. Bai, Z. Lu, J. Yang, Citrate-based tannin-bridged bone composites for lumbar fusion, *Adv. Funct. Mater.* 30 (27) (2020), <https://doi.org/10.1002/adfm.202002438>.
- [18] H. Zhou, J. Zhou, T. Wang, J. Zeng, L. Liu, J. Jian, Z. Zhou, L. Zeng, Q. Liu, G. Liu, In-situ preparation of silver salts/collagen fiber hybrid composites and their photocatalytic and antibacterial activities, *J. Hazard. Mater.* 359 (2018) 274–280, <https://doi.org/10.1016/j.jhazmat.2018.07.043>.
- [19] M. Zhu, X. Liu, L. Tan, Z. Cui, Y. Liang, Z. Li, K.W. Kwok Yeung, S. Wu, Photo-responsive chitosan/Ag/MoS₂ for rapid bacteria-killing, *J. Hazard. Mater.* 383 (2020) 121122.
- [20] B. Liang, E. Jia, X. Yuan, G. Zhang, Z. Su, Salt-responsive polyzwitterion brushes conjugated with silver nanoparticles: Preparation and dual antimicrobial/release properties, *Chem. Eng. J.* 401 (2020), <https://doi.org/10.1016/j.cej.2020.126114>.
- [21] X. Wang, G. Herting, I.O. Wallinder, E. Blomberg, Adsorption of bovine serum albumin on silver surfaces enhances the release of silver at pH neutral conditions, *PCCP* 17 (28) (2015) 18524–18534, <https://doi.org/10.1039/c5cp02306h>.
- [22] J.S. House, E. Bouzos, K.M. Fahy, V.M. Francisco, D.T. Lloyd, F.A. Wright, A. A. Motsinger-Reif, P. Asuri, K.E. Wheeler, Low-Dose Silver Nanoparticle Surface Chemistry and Temporal Effects on Gene Expression in Human Liver Cells, *Small* 16 (21) (2020) e2000299.
- [23] O. Pryshecha, P. Pomastowski, B. Buszewski, Silver nanoparticles: Synthesis, investigation techniques, and properties, *Adv. Colloid Interface Sci.* 284 (2020), 102246, <https://doi.org/10.1016/j.cis.2020.102246>.
- [24] J. Pandiarajan, M. Krishnan, Properties, synthesis and toxicity of silver nanoparticles, *Environ. Chem. Lett.* 15 (3) (2017) 387–397, <https://doi.org/10.1007/s10311-017-0624-4>.
- [25] B.B. Manshian, C. Pfeiffer, B. Pelaz, T. Heimerl, M. Gallego, M. Möller, P. del Pino, U. Himmelreich, W.J. Parak, S.J. Soenen, High-Content Imaging and Gene Expression Approaches To Unravel the Effect of Surface Functionality on Cellular Interactions of Silver Nanoparticles, *ACS Nano* 9 (10) (2015) 10431–10444, <https://doi.org/10.1021/acsnano.5b04661>.

- [26] D.-H. Lim, J. Jang, S. Kim, T. Kang, K. Lee, I.-H. Choi, The effects of sub-lethal concentrations of silver nanoparticles on inflammatory and stress genes in human macrophages using cDNA microarray analysis, *Biomaterials* 33 (18) (2012) 4690–4699, <https://doi.org/10.1016/j.biomaterials.2012.03.006>.
- [27] S.E. Orr, K. Gokulan, M. Boudreau, C.E. Cerniglia, S. Khare, Alteration in the mRNA expression of genes associated with gastrointestinal permeability and ileal TNF- α secretion due to the exposure of silver nanoparticles in Sprague-Dawley rats, *J. Nanobiotechnol.* 17 (1) (2019), <https://doi.org/10.1186/s12951-019-0499-6>.
- [28] P. Xiong, X. Huang, N. Ye, Q. Lu, G. Zhang, S. Peng, H. Wang, Y. Liu, Cytotoxicity of Metal-Based Nanoparticles: From Mechanisms and Methods of Evaluation to Pathological Manifestations, *Adv. Sci. (Weinh)* 9 (16) (2022) e2106049.
- [29] A. Sun, Z. Ban, L. Mu, X. Hu, Screening Small Metabolites from Cells as Multifunctional Coatings Simultaneously Improves Nanomaterial Biocompatibility and Functionality, *Adv. Sci. (Weinh)* 5 (7) (2018) 1800341, <https://doi.org/10.1002/advs.201800341>.
- [30] Z. Jia, M. Wen, Y. Cheng, Y. Zheng, Strategic Advances in Spatiotemporal Control of Bioinspired Phenolic Chemistries in Materials Science, *Adv. Funct. Mater.* 31 (14) (2021), <https://doi.org/10.1002/adfm.202008821>.
- [31] Y. Guo, Q. Sun, F.G. Wu, Y. Dai, X. Chen, Polyphenol-Containing Nanoparticles: Synthesis, Properties, and Therapeutic Delivery, *Adv. Mater.* 33 (22) (2021) e2007356.
- [32] S. Quideau, D. Deffieux, C. Douat-Casassus, L. Pouysegou, Plant polyphenols: chemical properties, biological activities, and synthesis, *Angew. Chem. Int. Ed. Engl.* 50 (3) (2011) 586–621, <https://doi.org/10.1002/anie.201000044>.
- [33] L.Q. Xu, K.-G. Neoh, E.-T. Kang, Natural polyphenols as versatile platforms for material engineering and surface functionalization, *Prog. Polym. Sci.* 87 (2018) 165–196, <https://doi.org/10.1016/j.progpolymsci.2018.08.005>.
- [34] Y. Li, Y. Miao, L. Yang, Y. Zhao, K. Wu, Z. Lu, Z. Hu, J. Guo, Recent Advances in the Development and Antimicrobial Applications of Metal-Phenolic Networks, *Adv. Sci.* 9 (27) (2022) 2202684.
- [35] Y. Fu, L. Yang, J. Zhang, J. Hu, G. Duan, X. Liu, Y. Li, Z. Gu, Polydopamine antibacterial materials, *Mater. Horiz.* 8 (6) (2021) 1618–1633, <https://doi.org/10.1039/d0mh01985b>.
- [36] H. Wang, X. Li, Y. Jiang, M. Li, Q. Xiao, T. Zhao, S. Yang, C. Qi, P. Qiu, J. Yang, Z. Jiang, W. Luo, A Universal Single-Atom Coating Strategy Based on Tannic Acid Chemistry for Multifunctional Heterogeneous Catalysis, *Angew. Chem. Int. Ed. Engl.* (2022) e202200465.
- [37] X. He, K. Gopinath, G. Sathishkumar, L. Guo, K. Zhang, Z. Lu, C. Li, E.T. Kang, L. Xu, UV-Assisted Deposition of Antibacterial Ag-Tannic Acid Nanocomposite Coating, *ACS Appl. Mater. Interfaces* 13 (17) (2021) 20708–20717, <https://doi.org/10.1021/acsmi.1c03566>.
- [38] O.V. Kharissova, H.V. Dias, B.I. Kharisov, B.O. Perez, V.M. Perez, The greener synthesis of nanoparticles, *Trends Biotechnol.* 31 (4) (2013) 240–248, <https://doi.org/10.1016/j.tibtech.2013.01.003>.
- [39] J.V. Buddingh, A. Hozumi, G. Liu, Liquid and liquid-like surfaces/coatings that readily slide fluids, *Prog. Polym. Sci.* 123 (2021), <https://doi.org/10.1016/j.progpolymsci.2021.101468>.
- [40] N. Erathodiyil, H.-M. Chan, H. Wu, J.Y. Ying, Zwitterionic polymers and hydrogels for antibiofouling applications in implantable devices, *Mater. Today* 38 (2020) 84–98, <https://doi.org/10.1016/j.mattod.2020.03.024>.
- [41] Y. Liu, R. Li, R. Xu, Y. Liu, Y. Wu, S. Ma, Z. Ma, X. Pei, F. Zhou, Repeatedly Regenerating Mechanically Robust Polymer Brushes from Persistent Initiator Coating (PIC), *Angew. Chem. Int. Ed.* 61 (26) (2022), <https://doi.org/10.1002/anie.202204410>.
- [42] Q. Wang, X. Pan, C. Lin, X. Ma, S. Cao, Y. Ni, Ultrafast gelling using sulfonated lignin-Fe³⁺ chelates to produce dynamic crosslinked hydrogel/coating with charming stretchable, conductive, self-healing, and ultraviolet-blocking properties, *Chem. Eng. J.* 396 (2020), <https://doi.org/10.1016/j.cej.2020.125341>.
- [43] Y. Wan, G. Feng, F.H. Shen, G. Balian, C.T. Laurencin, X. Li, Novel biodegradable poly(1,8-octanediol malate) for annulus fibrosus regeneration, *Macromol. Biosci.* 7 (11) (2007) 1217–1224, <https://doi.org/10.1002/mabi.200700053>.
- [44] B. Yang, Y. Chen, J. Shi, Reactive Oxygen Species (ROS)-Based Nanomedicine, *Chem. Rev.* 119 (8) (2019) 4881–4985, <https://doi.org/10.1021/acs.chemrev.8b00626>.
- [45] T. Wang, Y. Li, E.J. Cornel, C. Li, J. Du, Combined Antioxidant-Antibiotic Treatment for Effectively Healing Infected Diabetic Wounds Based on Polymer Vesicles, *ACS Nano* 15 (5) (2021) 9027–9038, <https://doi.org/10.1021/acsnano.1c02102>.
- [46] Q. He, S. Yuan, H. Tang, S.i. Wang, Z. Mu, D. Li, S. Wang, X. Jing, S. Hu, P. Ji, T. Chen, Safeguarding Osteointegration in Diabetic Patients: A Potent “Chain Armor” Coating for Scavenging ROS and Macrophage Reprogramming in a Microenvironment-Responsive Manner, *Adv. Funct. Mater.* 31 (31) (2021) 2101611.
- [47] Y. Sun, X. Sun, X. Li, W. Li, C. Li, Y. Zhou, L. Wang, B. Dong, A versatile nanocomposite based on nanoceria for antibacterial enhancement and protection from aPDT-aggravated inflammation via modulation of macrophage polarization, *Biomaterials* 268 (2021), 120614, <https://doi.org/10.1016/j.biomaterials.2020.120614>.
- [48] N. El Yamani, E. Mariussen, M. Gromelski, E. Wyrzykowska, D. Grabarek, T. Puzyn, S. Tanasescu, M. Dusinska, E. Rundén-Pran, Hazard identification of nanomaterials: In silico unraveling of descriptors for cytotoxicity and genotoxicity, *Nano Today* 46 (2022), <https://doi.org/10.1016/j.nantod.2022.101581>.
- [49] L. Ge, Q. Li, M. Wang, J. Ouyang, X. Li, M.M. Xing, Nanosilver particles in medical applications: synthesis, performance, and toxicity, *Int. J. Nanomed.* 9 (2014) 2399–2407, <https://doi.org/10.2147/IJN.S55015>.
- [50] J.L. Wu, Q.P. Wu, J.M. Zhang, R. Chen, M. Cai, J.B. Tan, Effects of L-Malate on Physical Stamina and Activities of Enzymes Related to the Malate-Aspartate Shuttle in Liver of Mice, *Physiol. Res.* 56 (2007) 213–220, <https://doi.org/10.33549/physiolres.930937>.
- [51] S. Nath, R. Elangovan, New perspectives on photosynthetic phosphorylation in the light of a torsional mechanism of energy transduction and ATP synthesis, *J. Bioenerg. Biomembr.* 43 (6) (2011) 601–610, <https://doi.org/10.1007/s10863-011-9396-x>.
- [52] Z.L. Dai, J. Wu, C. Meng, F. Zeng, Y. Yang, S.L. Yao, Ringer’s malate solution protects against the multiple organ injury and dysfunction caused by hemorrhagic shock in rats, *Shock* 38 (3) (2012) 268–274, <https://doi.org/10.1097/SHK.0b013e318264e664>.
- [53] C. Li, C. He, Y. Xu, H. Xu, Y. Tang, H. Chavan, S. Duan, A. Artigues, M.L. Forrest, P. Krishnamurthy, S. Han, J.M. Holzbeierlein, B. Li, Alternol eliminates excessive ATP production by disturbing Krebs cycle in prostate cancer, *Prostate* 79 (6) (2019) 628–639, <https://doi.org/10.1002/pros.23767>.
- [54] A.L. Byrd, Y. Belkaid, J.A. Segre, The human skin microbiome, *Nat. Rev. Microbiol.* 16 (3) (2018) 143–155, <https://doi.org/10.1038/nrmicro.2017.157>.
- [55] D. Triwongwanat, W. Boonchai, C. Subchookul, P. Sitthiamsuwan, R. Thuangtong, Synthetic hair reactions and treatment of complications: Case reports, *J. Cosmet. Dermatol.* 19 (10) (2020) 2697–2700, <https://doi.org/10.1111/jocd.13318>.
- [56] P. Seng, S. Bayle, A. Alliez, F. Romain, D. Casanova, A. Stein, The microbial epidemiology of breast implant infections in a regional referral centre for plastic and reconstructive surgery in the south of France, *Int. J. Infect. Dis.* 35 (2015) 62–66, <https://doi.org/10.1016/j.ijid.2015.04.010>.
- [57] M.D.M. Cendra, E. Torrents, *Pseudomonas aeruginosa* biofilms and their partners in crime, *Biotechnol. Adv.* 49 (2021), 107734, <https://doi.org/10.1016/j.biotechadv.2021.107734>.
- [58] M.S. Smetzer, *Staphylococcus aureus* Pathogenesis: The Importance of Reduced Cytotoxicity, *Trends Microbiol.* 24 (9) (2016) 681–682, <https://doi.org/10.1016/j.tim.2016.07.003>.
- [59] E. Unal Turhan, S. Polat, Z. Erginkaya, G. Konuray, Investigation of synergistic antibacterial effect of organic acids and ultrasound against pathogen biofilms on lettuce, *Food Biosci.* 47 (2022), <https://doi.org/10.1016/j.fbio.2022.101643>.
- [60] R. Chauhan, S. Kumari, G. Goel, W. Azmi, Synergistic combination of malic acid with sodium hypochlorite impairs biofilm of *Cronobacter sakazakii*, *Lwt* 155 (2022), <https://doi.org/10.1016/j.lwt.2021.112902>.
- [61] C. Marques, A.R. Sotiles, F.O. Farias, G. Oliveira, M.L. Mitterer-Daltoé, M. L. Masson, Full physicochemical characterization of malic acid: Emphasis in the potential as food ingredient and application in pectin gels, *Arab. J. Chem.* 13 (12) (2020) 9118–9129, <https://doi.org/10.1016/j.arabj.2020.10.036>.
- [62] Y. Jian, X. Chen, T. Ahmed, Q. Shang, S. Zhang, Z. Ma, Y. Yin, Toxicity and action mechanisms of silver nanoparticles against the mycotoxin-producing fungus *Fusarium graminearum*, *J. Adv. Res.* 38 (2022) 1–12, <https://doi.org/10.1016/j.jare.2021.09.006>.
- [63] H. Keum, T.W. Kim, Y. Kim, C. Seo, Y. Son, J. Kim, D. Kim, W. Jung, C.H. Whang, S. Jon, Bilirubin nanomedicine alleviates psoriatic skin inflammation by reducing oxidative stress and suppressing pathogenic signaling, *J. Control. Release* 325 (2020) 359–369, <https://doi.org/10.1016/j.jconrel.2020.07.015>.
- [64] C. Jia, D. Cao, S. Ji, X. Zhang, B. Muhoza, Tannic acid-assisted cross-linked nanoparticles as a delivery system of eugenol: The characterization, thermal degradation and antioxidant properties, *Food Hydrocoll.* 104 (2020), <https://doi.org/10.1016/j.foodhyd.2020.105717>.
- [65] Z. Hussain, I. Ullah, X. Liu, W. Shen, P.i. Ding, Y. Zhang, T. Gao, M. Mansoorianfar, T. Gao, R. Pei, Tannin-reinforced iron substituted hydroxyapatite nanorods functionalized collagen-based composite nanofibrous coating as a cell-instructive bone-implant interface scaffold, *Chem. Eng. J.* 438 (2022), <https://doi.org/10.1016/j.cej.2022.135611>.
- [66] Z. Wei, L. Wang, C. Tang, S. Chen, Z. Wang, Y. Wang, J. Bao, Y.i. Xie, W. Zhao, B. Su, C. Zhang, Metal-Phenolic Networks Nanoplatfrom to Mimic Antioxidant Defense System for Broad-Spectrum Radical Eliminating and Endotoxemia Treatment, *Adv. Funct. Mater.* 30 (49) (2020), <https://doi.org/10.1002/adfm.202002234>.
- [67] J.L. Wu, Q.P. Wu, Y.P. Peng, J.M. Zhang, Effects of L-malate on mitochondrial oxidoreductases in liver of aged rats, *Phys. Res.* 60 (2) (2011) 329–336, <https://doi.org/10.33549/physiolres.931986>.
- [68] S. Liu, Q. Zhang, J. Yu, N. Shao, H. Lu, J. Guo, X. Qiu, D. Zhou, Y. Huang, Absorbable Thioether Grafted Hyaluronic Acid Nanofibrous Hydrogel for Synergistic Modulation of Inflammation Microenvironment to Accelerate Chronic Diabetic Wound Healing, *Adv. Healthc. Mater.* 9 (11) (2020) e2000198.
- [69] G. Wang, E. Sweren, H. Liu, E. Wier, M.P. Alphonse, R. Chen, N. Islam, A. Li, Y. Xue, J. Chen, S. Park, Y. Chen, S. Lee, Y. Wang, S. Wang, N.K. Archer, W. Andrews, M.A. Kane, E. Dare, S.K. Reddy, Z. Hu, E.A. Grice, L.S. Miller, L. A. Garza, Bacteria induce skin regeneration via IL-1 β signaling, *Cell Host Microbe* 29 (5) (2021) 777–791 e6, <https://doi.org/10.1016/j.chom.2021.03.003>.
- [70] L. Liu, X. Xiao, K. Li, X. Li, K. Yu, X. Liao, B. Shi, Prevention of Bacterial Colonization Based on Self-Assembled Metal-Phenolic Nanocoating from Rare-

- Earth Ions and Catechin, ACS Appl. Mater. Interfaces 12 (19) (2020) 22237–22245, <https://doi.org/10.1021/acsami.0c06459>.
- [71] Z. Zhu, Q. Gao, Z. Long, Q. Huo, Y. Ge, N. Vianney, N.A. Daliko, Y. Meng, J. Qu, H. Chen, B. Wang, Polydopamine/poly(sulfobetaine methacrylate) Co-deposition coatings triggered by CuSO₄/H₂O₂ on implants for improved surface hemocompatibility and antibacterial activity, Bioact. Mater. 6 (8) (2021) 2546–2556, <https://doi.org/10.1016/j.bioactmat.2021.01.025>.
- [72] D. Zhang, Q. Chen, Y. Bi, H. Zhang, M. Chen, J. Wan, C. Shi, W. Zhang, J. Zhang, Z. Qiao, J. Li, S. Chen, R. Liu, Bio-inspired poly-DL-serine materials resist the foreign-body response, Nat. Commun. 12 (1) (2021) 5327, <https://doi.org/10.1038/s41467-021-25581-9>.